On Dysprosium Utilisation in Multi-main-phase Nd–Dy–Fe–B Magnets with Core–shell Microstructures

Zhiheng Zhang[a,+], Hansheng Chen[b,+], Jiaying Jin[a,*], Bryan Lim[b,1], Xiaolian Liu[c], Guohua Bai[c], Wei Li[d], Mi Yan[a], and Simon P. Ringer[b,*]

[a]School of Materials Science and Engineering, State Key Laboratory of Silicon materials, Key Laboratory of Novel Materials for Information Technology of Zhejiang Province, Zhejiang University, Hangzhou 310027, China

[b]School of Aerospace, Mechanical and Mechatronic Engineering, and Australian Centre for Microscopy and Microanalysis, The University of Sydney, NSW 2006, Australia

[c]Institute of Advanced Magnetic Materials, College of Materials and Environmental Engineering, Hangzhou Dianzi University, Hangzhou 310012, China

[d]School of Materials Science and Engineering, Nanchang Hangkong University, Nanchang 330063, China

[+]These authors contributed equally to this work.

*Corresponding authors. jinjy@zju.edu.cn (J. Jin); simon.ringer@sydney.edu.au (S. P. Ringer)

[1] Presently at the Materials Science and Technology Division, Oak Ridge National Laboratory, Knoxville, TN, USA

Abstract

The development of high-performance Nd–Dy–Fe–B magnets that minimise the consumption of scarce rare earth (RE) element Dy has been a major pursuit for both industry and academia. Here, we designed an alloy microstructure comprising of a uniform Dy-lean core–Dy-rich shell in a series of multi-main-phase (MMP) Nd–Dy–Fe–B magnets. Assessed by the increment of the coercivity and remanent magnetisation per unit weight percentage of the Dy addition ($\Delta\mu_0 H_c/\Delta$Dy and $\Delta\mu_0 M_r/\Delta$Dy), the resulting MMP Dy1 and Dy3 magnets with an overall Dy level of 1 and 3 wt.% possessed respective $\Delta\mu_0 H_c/\Delta$Dy values of 0.5 and 0.3 T/wt.%, and identical $\Delta\mu_0 M_r/\Delta$Dy values of -0.01 T/wt.%. Most importantly, the resulting MMP Dy3 magnet exhibited a high coercivity (2.4 T), the excellent thermal stability of coercivity ($|\beta|$ = 0.531%/°C), a high squareness factor (> 95%), with a little diminishment in the remanent magnetisation (1.35 T) and maximum energy product (43.6 MGOe). These properties are superior to the currently available sintered Nd–Dy–Fe–B magnets which utilise higher levels of Dy of 5 wt.%. Via multi-scale microstructural characterisation data with micromagnetic simulations, the formation of the Dy-lean core–Dy-rich shell microstructure is rationalised via solid-state-diffusion and solution reprecipitation during liquid-phase sintering. The Dy-lean core–Dy-rich shell microstructure and the non-ferromagnetic low-Fe RE-rich grain boundary phase enable synergistic magnetic performance. The present work establishes a pathway for the more sustainable utilisation of Dy in permanent magnets via forming the uniform Dy-lean core–Dy-rich shell microstructure.

Keywords: Permanent magnets, Multi-main-phase Nd–Dy–Fe–B, Core–shell microstructure, Liquid-phase sintering, Coercivity

1. Introduction

Rare earth (RE) elements remain both in the headlines of the critical metals agenda and the subject of intense research interest owing to their unique 4f electronic structure and physicochemical characteristics [1,2]. For example, an important class of RE-based materials is the sintered Nd–Dy–Fe–B magnet, which has experienced enormous recent demand due to the flourishing renewable energy technology markets [3-5]. Since the magnetocrystalline anisotropy field ($\mu_0 H_A$) of the $Dy_2Fe_{14}B$ phase (~15.0 T) is double that of the $Nd_2Fe_{14}B$ phase (~7.3 T) [6], the sintered Nd–Dy–Fe–B magnets exhibit higher coercivity ($\mu_0 H_c$) than the Dy-free Nd–Fe–B ones. High coercivity is a prerequisite for high-temperature applications of these materials beyond 150 °C [7,8]. Unfortunately, the sintered Nd–Dy–Fe–B magnets suffer from an inferior remanent magnetisation ($\mu_0 M_r$) and correspondingly lower maximum energy product [$(BH)_{max}$]. For example, a 3 wt.% Dy addition resulted in a decreased $\mu_0 M_r$ value from 1.35 to 1.19 T, and a $(BH)_{max}$ value from 38.0 to 34.5 MGOe [9,10]. It is widely agreed that the decrease of $\mu_0 M_s$ and the corresponding enhancement of $\mu^0 H^A = \frac{2K_1}{\mu_0 M_s}$ were caused primarily by the anti-ferromagnetic coupling between the Dy and Fe atoms in the $(Nd,Dy)_2Fe_{14}B$ phase [11,12].

There is another concern in the use of sintered Nd–Dy–Fe–B magnets from the viewpoint of cost performance and sustainability. This concern arises from the fact that Dy has been categorised as the most critical and threatened strategic metal [13,14]. Approximately 95% of the total annual consumption of Dy has been used to produce sintered Nd–Dy–Fe–B magnets since 2011 [15]. The coincidence between the sudden and heavy Dy dependence in energy markets, the limited geological distribution, and the scarce natural abundance is widely touted to herald the onset of a global Dy shortage in the coming decades [15,16]. Therefore, the minimisation of the Dy levels in high-performance sintered Nd–Dy–Fe–B magnets has emerged as a major research focus in recent years.

One of the common approaches is the dual-alloy method, firstly proposed by *M. Honshima et al.*, which comprised a $RE_2Fe_{14}B$ alloy and a Dy-bearing RE-rich alloy [17]. This approach aimed to achieve a uniform Dy-lean core–Dy-rich shell microstructure to minimise the use of

Dy in the fabrication of high-performance Nd–Dy–Fe–B magnets. More attempts were conducted later in searching for the optimised concentrations of the Dy-bearing RE-rich alloys, e.g., Dy [18], DyH_x [19], (Pr, Dy, Cu)H_x [20], DyF_3 [21], Dy_2S_3 [22], Dy_2O_3 [22], Dy-Fe [23], Dy-Ni [24], Dy-Al [25], and Dy-Co [26]. However, the major problem is still the relatively lower $\mu_0 M_r$ and $(BH)_{max}$ values.

The dual-alloy method was subsequently developed, utilising two Dy-bearing $RE_2Fe_{14}B$-type alloys with varying RE concentrations [27]. This is also referred to as the "multi-main-phase (MMP) method" due to the attainment of the $RE_2Fe_{14}B$ phases with various RE concentrations. Though there were a few attempts later [28-31], the mechanism for the formation of the Dy-lean core–Dy-rich shell microstructure remains largely unexplored in the MMP Nd–Dy–Fe–B magnets. The partitioning, segregation, and diffusional phenomena of the alloying elements (particularly Dy) during liquid-phase sintering remain elusive, due to the lack of the high-resolution microstructural characterisation. This is crucial for accurate microstructure control when designing the Dy-lean core–Dy-rich shell microstructure in the MMP Nd–Dy–Fe–B magnets.

In this work, we presented a materials design implementation that delivers the first variation of the Dy concentrations of the initial magnetic powders, and a concomitant optimisation of the sintering and annealing temperatures to liberate the best combination of $\mu_0 H_c$, $\mu_0 M_r$, $(BH)_{max}$, squareness factor (SF), thermal stability of coercivity $|\beta|$ and remanent magnetisation $|\alpha|$ reported-to-date in the MMP Nd–Dy–Fe–B magnets. Using atomic-scale microstructural characterisation, we revealed the Dy-lean core–Dy-rich shell microstructure and the elemental distribution (particularly Dy) at the intergranular grain boundaries and at the $RE_2Fe_{14}B$ grain surfaces. We also proposed a two-step mechanism, accounting for the formation and the absence of the core–shell microstructures in our MMP Nd–Dy–Fe–B magnets.

2. Experimental

2.1. Materials Processing

Four batches of the initial magnetic powders with a mean particle size of ~3.3 μm were prepared by induction melting, strip casting, hydrogen decrepitating, and jet milling. Their respective nominal compositions were $(Nd_{80}Pr_{20})_{30.5}Fe_{bal}M_{1.3}B_{1.0}$, $[(Nd_{80}Pr_{20})_{0.75}Dy_{0.25}]_{30.5}Fe_{bal}M_{1.3}B_{1.0}$, $[(Nd_{80}Pr_{20})_{0.50}Dy_{0.50}]_{30.5}Fe_{bal}M_{1.3}B_{1.0}$, and $[(Nd_{80}Pr_{20})_{0.25}Dy_{0.75}]_{30.5}Fe_{bal}M_{1.3}B_{1.0}$ (M = Cu, Al, Ga, Zr, Co, wt.%), hereafter referred to as Dy0, Dy25, Dy50, and Dy75 powders, respectively. According to **Table S1**, the fraction of the RE-rich phase remained similar for the Dy0, Dy25, and Dy50 powders (~2 wt.%), which however increased to 4.59 wt.% for the Dy75 powders. Therefore, the magnetic powders with even higher Dy concentration, such as Dy100, were not prepared. The magnetic properties of the MMP Dy3 magnets with an overall Dy level of 3 wt.% processed from the Dy0–Dy25, Dy0–Dy50, and Dy0–Dy50 powder mixtures (designated as MMP Dy3-I, MMP Dy3-II, and MMP Dy3-III magnets, respectively) were firstly measured. **Fig. S1** and **Table S2** showcase that the MMP Dy3-III magnet possessed the highest $\mu_0 H_c$ and $\mu_0 M_r$ values among these three magnets. Therefore, the combination of the Dy0 and Dy75 powders were down-selected for further research.

Next, the Dy0 and Dy75 powders were mixed with the Dy75 mass ratios of 0, 4.37%, 8.74%, 13.11%, 17.48%, and 21.85%. The resulting powder mixtures possessed the compositions of $(Nd_{80}Pr_{20})_{30.5-x}Dy_xFe_{bal}M_{1.3}B_{1.0}$ where x = 0, 1, 2, 3, 4, 5 wt.%, accordingly designated as Dy0, Dy1, Dy2, Dy3, Dy4, and Dy5 powder mixtures. Under a nitrogen atmosphere where the oxygen levels were monitored below 50 ppm, the Dy0–Dy5 powder mixtures were then aligned in a magnetic field of 1.6 T and compacted under 5.5 MPa. The aligned green compacts possessed a dimension of ~70 × 43 (compacting direction) × 54 (aligning direction) mm^3. These aligned green compacts were then vacuum sealed in plastic envelopes and subjected to isostatic pressing under 200 MPa. These pressed magnets were further sintered (1075 °C for 3 h) and two-step annealed (890 °C for 3 h, and 490 °C for 4.5 h) in a vacuum furnace under a pressure $\leqslant 1\times10^{-3}$ Pa, and were designated as as-sintered and

post-sinter annealed Dy0 and MMP Dy1–Dy5 magnets. Due to the dimensional shrinkage occurred during liquid-phase sintering, the post-sintered annealed Dy0 and MMP Dy1–5 magnets possessed a dimension of ~55 × 35 × 40 mm^3. The liquid-phase sintering and 2nd annealing temperatures used here were optimised carefully (**Tables S3 and S4, Figs. S2 and S3**). The compositions of the post-sinter annealed magnets were measured by inductively coupled plasma–atomic emission spectroscopy (ICP–AES) and provided in **Table S5**.

2.2. Magnetic property measurements

The magnetic properties of the post-sinter annealed Dy0 and MMP Dy1–Dy5 magnets were measured upon elevated temperature from 20 to 180 °C using a NIM-62000 hysteresigraph analyzer. The thermal coefficients of $\mu_0 H_c$ ($|\beta|$) and $\mu_0 M_r$ ($|\alpha|$) in the various temperature intervals were calculated using the following equations: $|\beta| = |\Delta\mu_0 H_c/(\mu_0 H_c \Delta T)| \times 100\%$ and $|\alpha| = |\Delta\mu_0 M_r/(\mu_0 M_r \Delta T)| \times 100\%$ [32].

2.3. Microscopy and Microanalysis

The post-sinter annealed Dy0, MMP Dy1 and Dy3 magnets were sectioned into slices to *in-situ* monitor the evolution of the magnetic domain structures by a magneto-optical Kerr microscope (Evico magnetics GmbH). All the slices with the *c* axis in the observation plane were magnetised to saturation under a pulse field of 7 T. A demagnetisating field was subsequently applied and increased until reaching 1.3 T.

Microstructural observations were conducted on the as-sintered and post-sinter annealed Dy0, MMP Dy1, Dy3, and Dy5 magnets using a scanning electron microscope (SEM, Hitachi S-3400N). Multiple backscattered electron (BSE) images were captured and imported into the Digimizer software to measure the size of the $RE_2Fe_{14}B$ grains. The results were plotted as frequency histograms with a bin size of 1 μm.

Elemental mapping was carried out on the post-sinter annealed MMP Dy1, Dy3, and Dy5 magnets using an electron probe microanalyzer (EPMA, Shimadzu-1720) via wavelength dispersive X-ray spectrometer (WDXS). X-ray diffraction experiments were conducted using

a Rigaku-S2 diffractometer with Cu K_α radiation. The local crystallographic texture of the post-sinter annealed MMP Dy3 magnet was assessed by a Zeiss ULTRA Plus SEM equipped with a complementary metal-oxide-semiconductor electron backscatter diffraction (EBSD) detector.

Transmission electron microscopy (TEM) lamellas were prepared from the post-sinter annealed Dy0 and MMP Dy3 magnets, using a dual beam-assisted site-specific lift-out technique [33]. Transmission electron microscopy (TEM) and scanning transmission electron microscopy–energy dispersive X-ray spectroscopy (STEM–EDXS) experiments were conducted on these TEM lamellas using a JEOL-2100F. Atom probe tomography (APT) experiments were conducted on the post-sinter annealed Dy0, MMP Dy3 and Dy5 magnets, using a CAMECA Local Electrode Atom Probe 4000X Si atom probe microscope equipped with a picosecond-pulse ultraviolet laser with a wavelength of 355 nm. The base temperature, laser frequency, and laser energy were selected to be 50 K, 200 kHz, and 50 or 100 pJ, respectively. Data reconstruction was performed via AP suite 6.1.0 and CAMECA Integrated Visualization & Analysis Software (IVAS) version 3.8.4. The error bars (σ_i) shown in the proximity histograms were calculated as: $\sigma_i = \sqrt{\frac{C^i(1 - C^i)}{N}}$, where $C_i = N_i/N$, N_i represents the number of i solute ions/atoms, and N represents the total number of all ions/atoms with the given bin [34,35]. The bin width was defined as 0.2 nm.

2.4. Micromagnetic simulations

To simulate the influence of the core–shell microstructures on the $\mu_0 H_c$ value, micromagnetic simulations were employed using a parallel finite element micromagnetic package (Magpar) [36,37]. The saturation magnetisation ($\mu_0 M_s$), magnetocrystalline anisotropy constant (K_1), and the exchange stiffness (A) of the $(Nd_{1-x}Dy_x)_2Fe_{14}B$ cores and the shells were linearly extrapolated from those values of the $Nd_2Fe_{14}B$ and $Dy_2Fe_{14}B$ phases [38-40]. For the $Nd_2Fe_{14}B$ phase, $\mu_0 M_s$ = 1.61 T, K_1 = 4.5 MJ/m^3, and A = 12.5 pJ/m [39]. For the $Dy_2Fe_{14}B$ phase, $\mu_0 M_s$ = 0.71 T, K_1 = 4.2 MJ/m^3, and A = 12.8 pJ/m [40]. The detailed concentrations of the $(Nd_{1-x}Dy_x)_2Fe_{14}B$ cores and the shells for each condition were estimated based on experimental EPMA results (**Table S6**).

3. Results

3.1. Macromagnetic properties

Fig. 1a provides the demagnetisation curves of the post-sinter annealed Dy0 and MMP Dy1–Dy5 magnets measured at ambient temperature (20 °C). The dependence of the $\mu_0 H_c$ and $\mu_0 M_r$ values on the Dy level is apparent from the plot provided in **Fig. 1**b, which can be categorised into two regimes. In the low-Dy-level regime (Dy level ≤ 3 wt.%), the $\mu_0 H_c$ value of the post-sinter annealed MMP Nd–Dy–Fe–B magnet was increased from 1.5 to 2.0 T with 1 wt.% Dy addition, and to 2.4 T with the increasing Dy level to 3 wt.%. The $\mu_0 M_r$ value was slightly decreased from 1.38 to 1.35 T correspondingly. The decrease of the $\mu_0 M_r$ value per unit weight percentage of the Dy addition was 0.01 T/wt.% Dy in the low-Dy-level regime.

In the high-Dy-level regime (Dy level > 3 wt.%), the $\mu_0 H_c$ value increment was limited to 0.2 T when the Dy level was further increased from 3 to 5 wt.%. The $\mu_0 M_r$ value decreased from 1.35 to 1.25 T in the high-Dy-level regime. This is a fivefold change as much as that in the low-Dy-level regime. Note that all the demagnetisation curves exhibit the single-phase-like behaviour with high SF values above 95.0%(**Table 1**), which enabled the high $(BH)_{max}$ values in the post-sinter annealed MMP Dy1–Dy5 magnets. Here, SF is defined as $\frac{\mu_0 H_k}{\mu_0 H_c}$ [41], where $\mu_0 H_k$ is defined as the knee reversed field at 90% of $\mu_0 M_r$.

TABLE 1. Mass ratio of the Dy75 powders used in the materials processing and the magnetic properties of the post-sinter annealed Dy0 and MMP Dy1–Dy5 magnets.

Magnets	Mass ratio of Dy75 powders	$\mu_0 M_r$ (T)	$\mu_0 H_c$ (T)	$(BH)_{max}$ (MGOe)	SF (%)
Dy0	0%	1.38	1.5	47.0	95.8
Dy1	4.37%	1.37	2.0	46.5	95.5
Dy2	8.74%	1.36	2.2	45.4	95.9
Dy3	13.11%	1.35	2.4	43.6	95.3

Dy4	17.48%	1.31	2.5	41.3	95.1
Dy5	21.85%	1.25	2.6	39.7	95.2

Fig. S4 provides the demagnetisation curves of the post-sinter annealed Dy0 and MMP Dy1–Dy5 magnets measured at the increasing temperature from 20 to 180 °C, with the corresponding $\mu_0 H_c$ values provided in **Fig. S5**. The absolute values of the temperature coefficients of $\mu_0 H_c$ ($|\beta|$) and $\mu_0 M_r$ ($|\alpha|$) in different temperature intervals are plotted in **Figs. 1**c and e. **Figs. 1**d and f provide the derived $|\beta|$ and $|\alpha|$ values measured in the typical temperature interval of 20–140 °C. A clear non-linear dependence of the $|\beta|$ value on the Dy level was observed, revealing that the $|\beta|$ value was lowered more rapidly in the low-Dy-level regime than in the high-Dy-level regime. Meanwhile, the $|\alpha|$ value was lowered in the low-Dy-level regime but increased in the high-Dy-level regime.

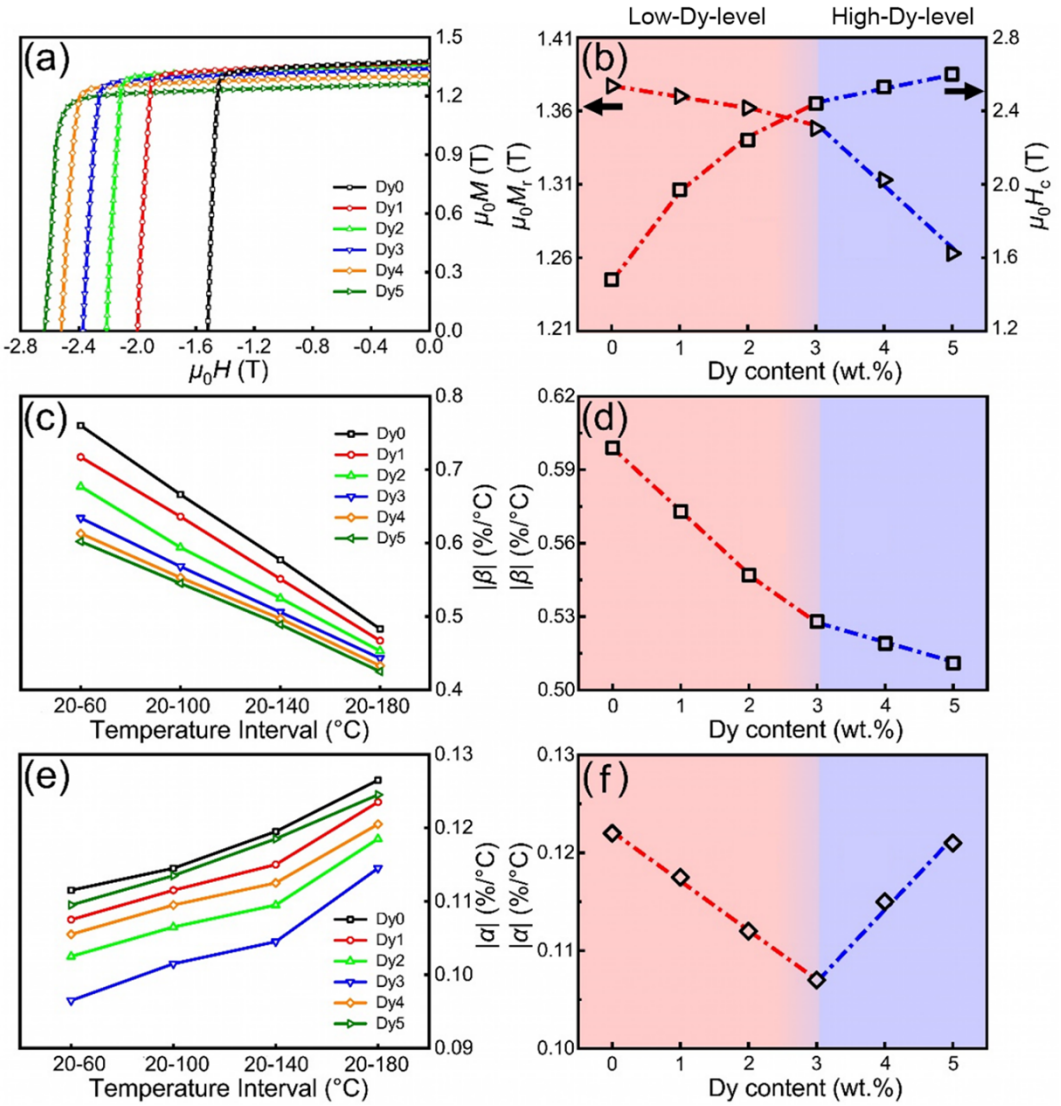

FIGURE 1. Magnetic properties of the post-sinter annealed Dy0 and multi-main-phase (MMP) Dy1–Dy5 magnets. (a) Demagnetisation curves measured at ambient temperature (20 °C). (b) The values of remanent magnetisation and coercivity as a function of the Dy level. Absolute values of the thermal coefficients of (c) coercivity $|\beta|$ and (e) remanent magnetisation $|\alpha|$ in different temperature intervals. The dependence of the (d) $|\beta|$ and (f) $|\alpha|$ values on the Dy level in the temperature interval of 20–140 °C.

Fig. 2a summarises magnetic properties of our post-sinter annealed MMP Dy1–Dy5 magnets (red), compared to a wide range of the commercial sintered (S), hot-deformed (HD), and grain boundary diffusion processed (GBDP) Nd–Dy–Fe–B magnets. Our post-sinter annealed MMP Dy3 magnet exhibit a unique combination of high $\mu_0 H_c$ and $\mu_0 M_r$ values ($\mu_0 H_c$

= 2.4 T and $\mu_0 M_r$ = 1.35 T) when compared to the traditional S–Dy3 magnets with the same Dy level ($\mu_0 H_c$ = 1.75 T, $\mu_0 M_r$ = 1.35 T) [42], and the nanocrystalline HD–Dy3.5 magnet ($\mu_0 H_c$ = 2.25 T, $\mu_0 M_r$ = 1.28 T) [43]. The $\mu_0 H_c$ value of the post-sinter annealed MMP Dy3 magnet was even higher than that of the traditional S–Dy5 magnet. **Fig. 2**a also demonstrates that the post-sinter annealed MMP Dy1–Dy3 magnets exhibited performance that was close to the GBDP Nd–Dy–Fe–B magnets that are used in low-melting-point Dy–*X* (*X* = Cu, Co, Al, etc.) [41,44-48], Dy–(H/F/O) sources [49-58], or Dy vapor/sputtering deposition [59-69]. These results reveal the potential of MMP processing to produce larger-scale (sections ≥ 10 mm) high-performance Nd–Dy–Fe–B magnets.

Figs. 2b and c further compare the increment of the $\mu_0 H_c$ and $\mu_0 M_r$ values per unit weight percentage of the Dy addition ($\Delta\mu_0 H_c/\Delta$Dy and $\Delta\mu_0 M_r/\Delta$Dy) at ambient temperature between our post-sinter annealed MMP Dy1–Dy5 magnets (red) and other reports using dual-alloy method [18-26,28-30]. In general, the $\Delta\mu_0 H_c/\Delta$Dy value is clearly reducing with the increasing Dy concentration. Our post-sinter annealed MMP Dy1 and Dy3 magnets possessed comparable $\Delta\mu_0 H_c/\Delta$Dy values (0.5 and 0.3 T/wt.%) to the previous works. Meantime, the decrease of the $\Delta\mu_0 M_r/\Delta$Dy values was merely 0.01 T/wt.% for the post-sinter annealed MMP Dy 1 and Dy3 magnets, which are relatively lower than the values of the previous works. Overall, our post-sinter annealed MMP Dy1 and Dy3 magnets possessed a better combination of the $\Delta\mu_0 H_c/\Delta$Dy and $\Delta\mu_0 M_r/\Delta$Dy values compared with the previous works using the dual-alloy method.

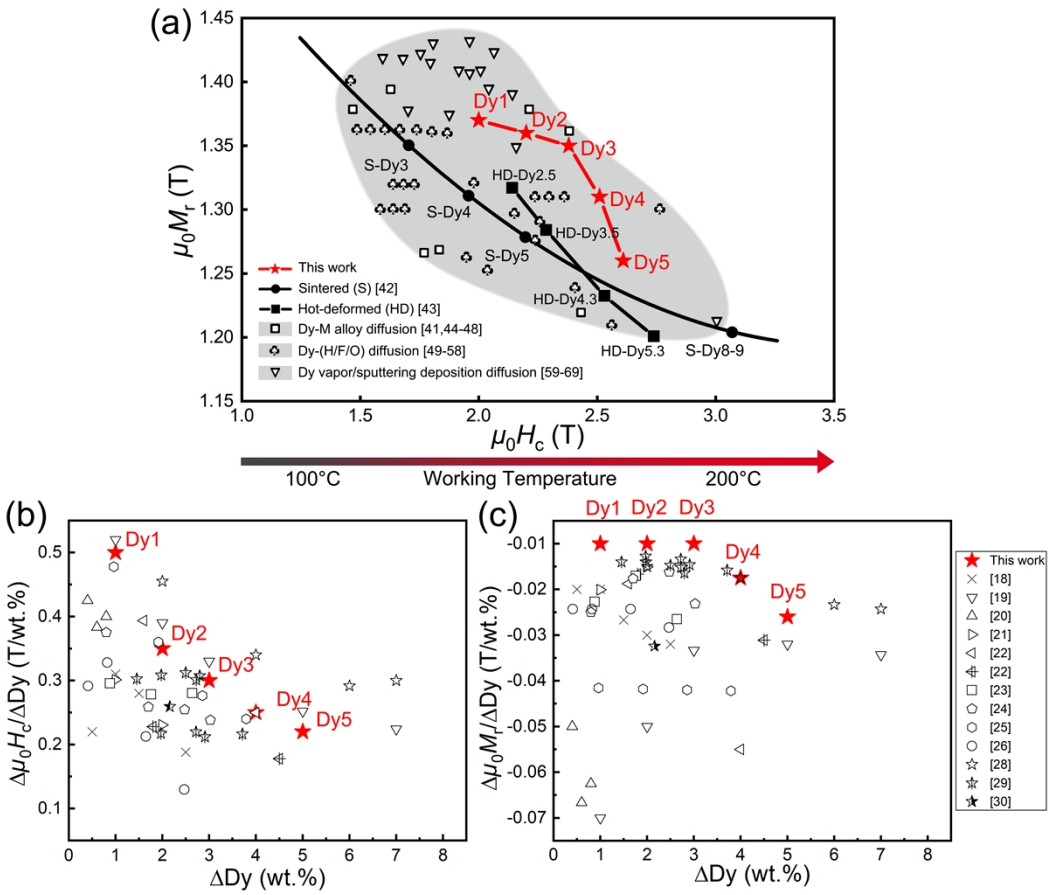

FIGURE 2. (a) Comparison of remanent magnetisation ($\mu_0 M_r$) versus coercivity ($\mu_0 H_c$) at ambient temperature between the post-sinter annealed MMP Dy1–Dy5 magnets (red) and previous reports of the sintered (S, solid circle) [42], hot-deformed (HD, solid square) [43], and grain boundary diffusion processed (GBDP, hollow symbols within the gray-shaded region) magnets [41,44-69]. Comparison of the increment of (b) $\mu_0 H_c$ and (c) $\mu_0 M_r$ value per unit weight percentage of the Dy addition at ambient temperature between the post-sinter annealed MMP Dy1–Dy5 magnets (red) and previous reports using dual-alloy method [18-26,28-30].

3.2. Evolution of the magnetic domain structure

To investigate the underlying mechanisms governing the excellent combination of the high $\mu_0 H_c$ and $\mu_0 M_r$ values across the low-Dy-level regime, the evolution of the magnetic domain structures of our post-sinter annealed Dy0, MMP Dy1 and Dy3 magnets were characterised (refer to the unprocessed datasets in **Fig. S6**). **Fig. 3**a is a schematic of the region where the magnetic domains were observed. **Fig. 3**b is a schematic of the subsequent

processing of the captured Kerr images. The processing involves the subtraction of the optical image contrast captured at the desired applied field (demagnetising field) from that captured at the maximum pulse field of 7 T. Note that the direction of the applied field was antiparallel to the direction of the maximum pulse field. The black and the white regions in the Kerr image (**Figs. 3**b-e) were referred to as the initial and reversed domains, respectively.

From left to right in **Figs. 3**c-e, the applied field was increased gradually from -0.3 to -1.3 T. For the post-sinter annealed Dy0 and MMP Dy1 magnets, the reversed domains nucleated at the applied field ≤ -0.3 T (**Figs. 3**b and c). The reversed domains were found to be constrained either at single $RE_2Fe_{14}B$ grain or a group of $RE_2Fe_{14}B$ grains upon demagnetisation. With the increasing applied field to -1.3 T, the fraction of the reversed domains was increased to ~82% and ~61% in the post-sinter annealed Dy0 and MMP Dy1 magnets, respectively. By contrast, the reversed domains in the post-sinter annealed MMP Dy3 magnet were not present until the applied field was increased beyond -1.2 T. The reversed domains nucleated and propagated rapidly, and reached ~46% of the areal fraction (**Figs. 3**d-e) at the applied field of -1.3 T. This demonstrates that the post-sinter annealed MMP Dy3 magnet possessed stronger resistance to the nucleation of the reversed domains than the Dy0 and Dy1 ones.

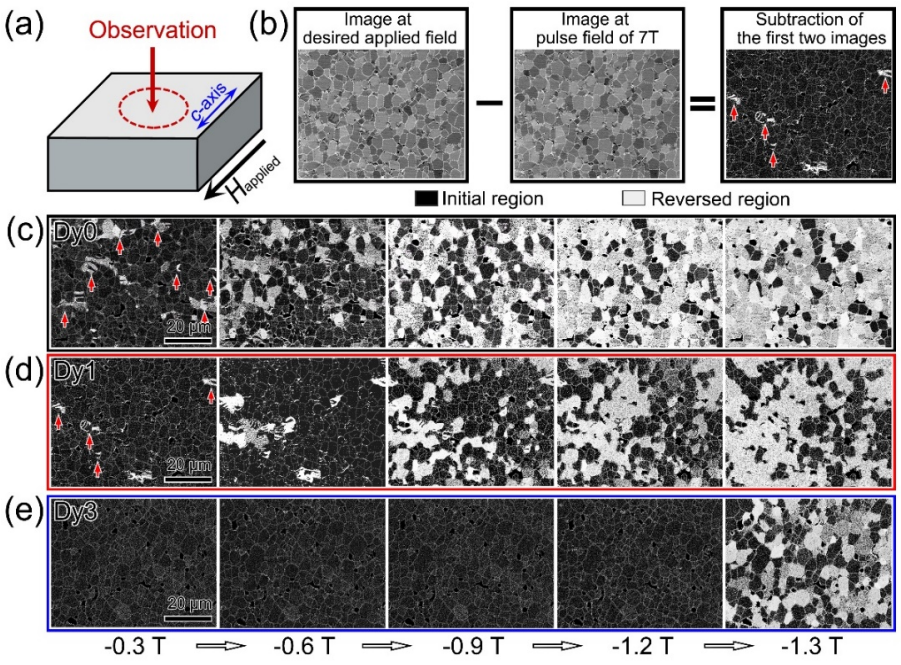

FIGURE 3. *In-situ* demagnetisation process for the post-sintered annealed Dy0, MMP Dy1 and Dy3 magnets. (a) Schematic of the region where the magnetic domains were observed by magneto-optical Kerr microscopy. (b) Subsequent subtraction processing of the Kerr images. Subtracted Kerr images showing the nucleation and propagation of the reversed domains (bright) in the post-sinter annealed (c) Dy0, (d) MMP Dy1, and (e) MMP Dy3 magnets under the increasing applied field.

3.3. Microstructural observations

3.3.1. Micron-scale characterisation

Advanced microscopy and microanalysis approaches were used to characterise the microstructure of the as-sintered and post-sinter annealed Dy0, MMP Dy1, Dy3, and Dy5 magnets at different length scales. **Fig. 4** provides backscattered electron (BSE) images of the as-sintered and post-sinter annealed Dy0, MMP Dy1, Dy3, and Dy5 magnets at the micron scale. The dark grey regions correspond to the $RE_2Fe_{14}B$ grains, while the bright regions correspond to the intergranular RE-rich triple junctions (TJs) or grain boundaries (GBs). There was no contrast difference within the $RE_2Fe_{14}B$ grains in the as-sintered Dy0 magnet, while a clear contrast was observed in the as-sintered MMP Dy1 and Dy3 magnets. 85–95% of the $RE_2Fe_{14}B$ grains possessed a core (darker)–shell (brighter) microstructure, designated as the Type I $RE_2Fe_{14}B$ grains. The remaining $RE_2Fe_{14}B$ grains exhibited the opposite core (brighter)–shell (darker) microstructure marked by the red arrows, designated as Type II $RE_2Fe_{14}B$ grains. In the as-sintered MMP Dy5 magnet, the fraction of the Type II $RE_2Fe_{14}B$ grains was increased greatly. Type I $RE_2Fe_{14}B$ grains were no longer present. Instead, the chemically uniform $RE_2Fe_{14}B$ grains were formed. Further comparative studies between the as-sintered and the post-sinter annealed MMP Dy1, Dy3, and Dy5 magnets indicated that the core–shell microstructures were essentially unchanged. However, more continuous intergranular RE-rich GBs were formed after post-sinter annealing (Refer to the enlarged view of the blue rectangles shown in **Fig. 4**b).

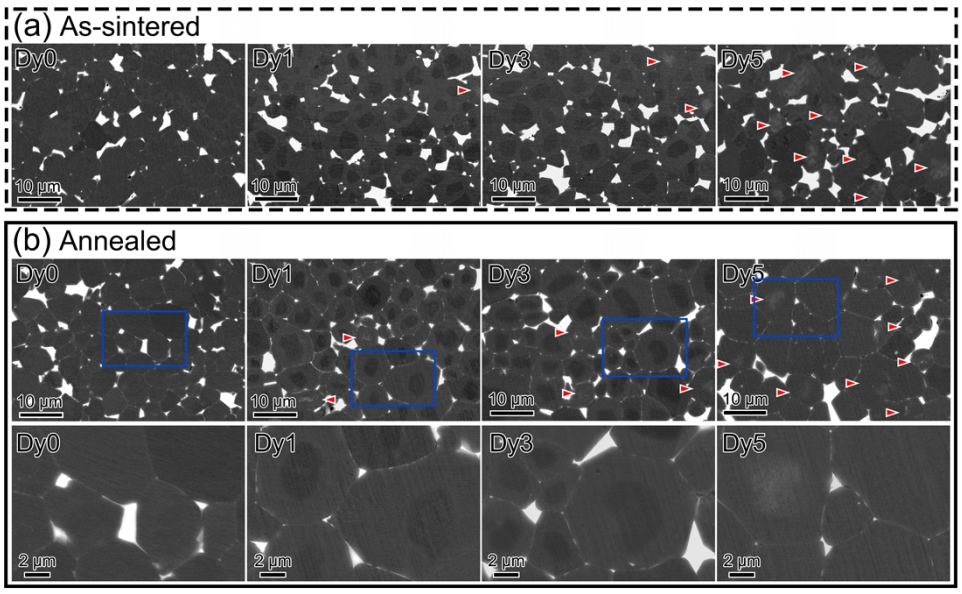

FIGURE 4. Backscattered electron (BSE) images of the (a) as-sintered, and (b) post-sinter annealed Dy0, MMP Dy1, Dy3, and Dy5 magnets. The bottom images refer to the blue rectangles shown in the BSE images for the post-sinter annealed magnets.

Fig. 5 provides a higher magnification BSE image and corresponding EPMA maps of the post-sinter annealed MMP Dy1, Dy3, and Dy5 magnets. Analogous to the MMP La/Ce/Y-based magnets [32,70-74], two types of the $RE_2Fe_{14}B$ grains were observed in the case of the post-sinter annealed MMP Dy1 and Dy3 magnets (**Figs. 5**a and b). The first type was comprised of a Dy-rich core and a Dy-lean shell, which correspond to the Type II $RE_2Fe_{14}B$ grain presented in **Fig. 4**. The second type consisted of a Dy-lean core and a Dy-rich shell, corresponding to the predominant Type I $RE_2Fe_{14}B$ grain. The WDXS line-scans revealed that the difference in the Dy concentration between the Dy-rich shells and the Dy-lean cores (ΔC) was ~2.9 and ~3.4 wt.% for the post-sinter annealed MMP Dy1 and Dy3 magnets, respectively. The higher ΔC value of ~3.4 wt.% suggested the well-developed Dy-lean core–Dy-rich shell microstructure in the post-sinter annealed MMP Dy3 magnet. For the post-sinter annealed MMP Dy5 magnet, the fraction of the Type II $RE_2Fe_{14}B$ grains was substantially increased (**Fig. 5**c), and the Type I $RE_2Fe_{14}B$ grains were no longer present, as verified by the WDXS line-scan result (ΔC_5 = ~0 wt.%). Thus, the intragranular RE compositional heterogeneity was initially enhanced and then weakened with the increasing Dy level from 0 to 5 wt.%.

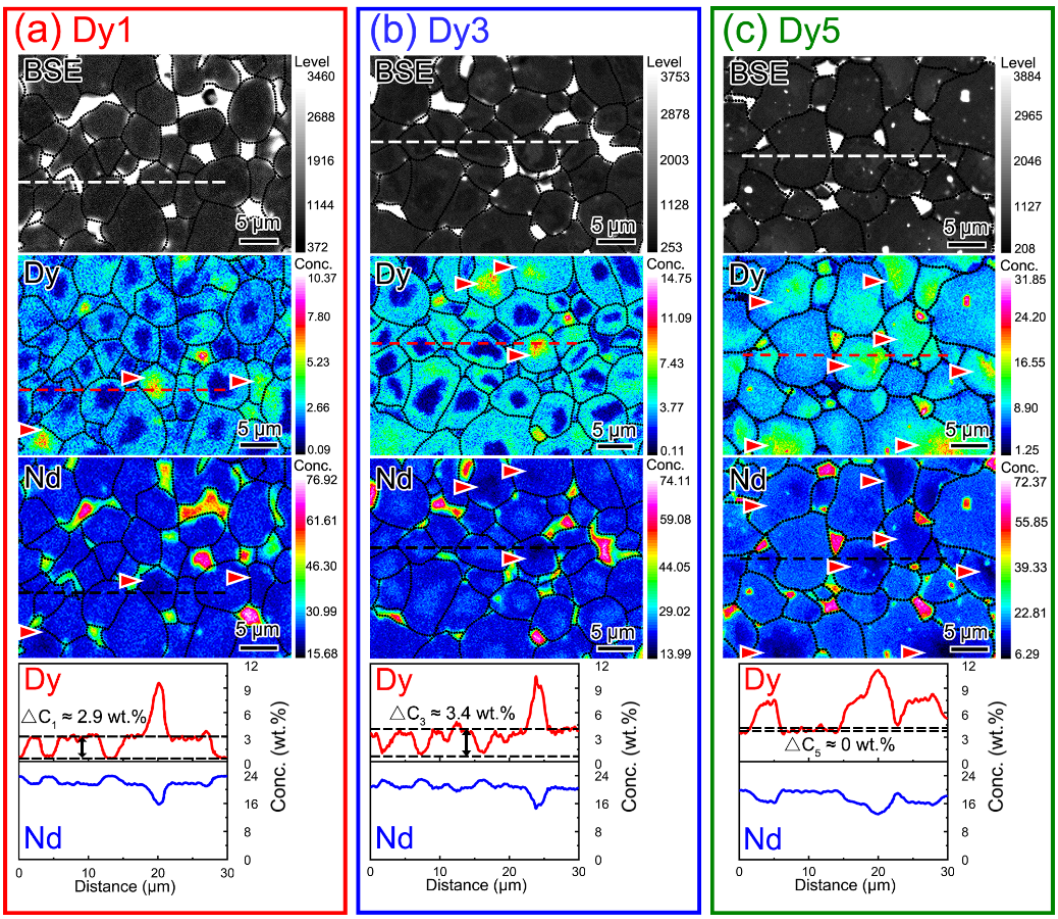

FIGURE 5. BSE image, elemental distribution maps by the electron probe microanalyser (EPMA), and plots of the wavelength dispersive X-ray spectrometer (WDXS) line-scans recorded from the post-sinter annealed MMP (a) Dy1, (b) Dy3, and (c) Dy5 magnets.

Fig. 6 provides the statistical distribution of the size of the $RE_2Fe_{14}B$ grains in the post-sinter annealed Dy0, MMP Dy1, Dy3, and Dy5 magnets. The average size of the $RE_2Fe_{14}B$ grains was increased from 4.1 to 5.1, 6.3, and 8.2 μm with the increasing Dy level from 0 to 1, 3, and 5 wt.%, accompanied with the increasing standard deviation from 1.6 to 2.1, 2.2, and 2.5 μm. The average sizes of the $RE_2Fe_{14}B$ grains recorded in the post-sinter annealed Dy0, MMP Dy1, Dy3, and Dy5 magnets were higher than that of the Dy0 and Dy75 powders of ~3.3 μm. This suggests the growth of the $RE_2Fe_{14}B$ grains occurred during materials processing.

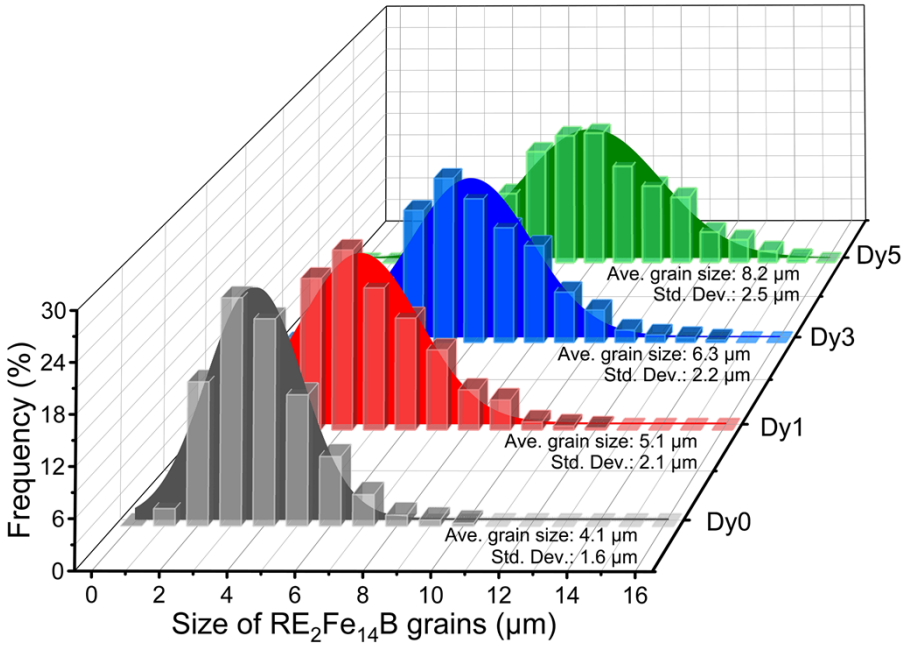

FIGURE 6. Plots of the frequency versus the size of the $RE_2Fe_{14}B$ grains in the post-sinter annealed Dy0, MMP Dy1, Dy3, and Dy5 magnets.

The grain growth with the increasing Dy levels was accompanied by an enhancement of the {001} texture, as verified by XRD and EBSD. In **Fig. 7**a, four major peaks were identified as the {004}, {105}, {006}, and {008} planes of the $RE_2Fe_{14}B$ grains. **Fig. 7**b displays the corresponding values for the peak intensity ratio of the {006} planes to the {105} planes, designated as $I_{\{006\}}/I_{\{105\}}$. With the increasing Dy level from 0 to 5 wt.%, the value of $I_{\{006\}}/I_{\{105\}}$ was increased from 0.95 to 1.32. **Fig. 7**c provides the {006} pole figures where the maximum value for the intensity appeared at the centre recorded by XRD. This indicates that the <001> directions (*c* axes) of the $RE_2Fe_{14}B$ grains were aligned parallel to the normal direction (Z) to form a strong {001} texture [75,76]. The maximum value was 9.2, 10.0, 11.6, and 14.0 in the post-sinter annealed Dy0, MMP Dy1, Dy3, and Dy5 magnets, respectively. The value for the intensity at the peripheral regions was found to be lower in the post-sinter annealed MMP Dy5 magnet compared with the Dy0, Dy1, and Dy3 ones. This indicates that the post-sinter annealed MMP Dy5 magnet possessed the fewest misaligned $RE_2Fe_{14}B$ grains.

To study whether there is crystallographic misorientation between the core and the shell of the $RE_2Fe_{14}B$ grains in the post-sinter annealed MMP Dy3 magnet, EBSD experiments were

additionally conducted. **Fig. 7**d provides the inverse pole figure (IPF)–Z of the $RE_2Fe_{14}B$ grains in the post-sinter annealed MMP Dy3 magnet. Note that the unindexed regions (black) correspond to the intergranular RE-rich TJs and GBs. The color imposed on each $RE_2Fe_{14}B$ grain represents its crystallographic orientation. The red color in **Fig. 7**d indicates that the *c* axes of the $RE_2Fe_{14}B$ grains were aligned well with the normal direction (Z). In other words, the strong {001} texture was formed in the post-sinter annealed MMP Dy3 magnet, in excellent agreement with the XRD findings (**Fig. 7**a-c). The misorientation angle was no more than 0.5° in both line–1 and line–2 (**Fig. 7**e), indicating the epitaxial relationship between the cores and the shells in these $RE_2Fe_{14}B$ grains.

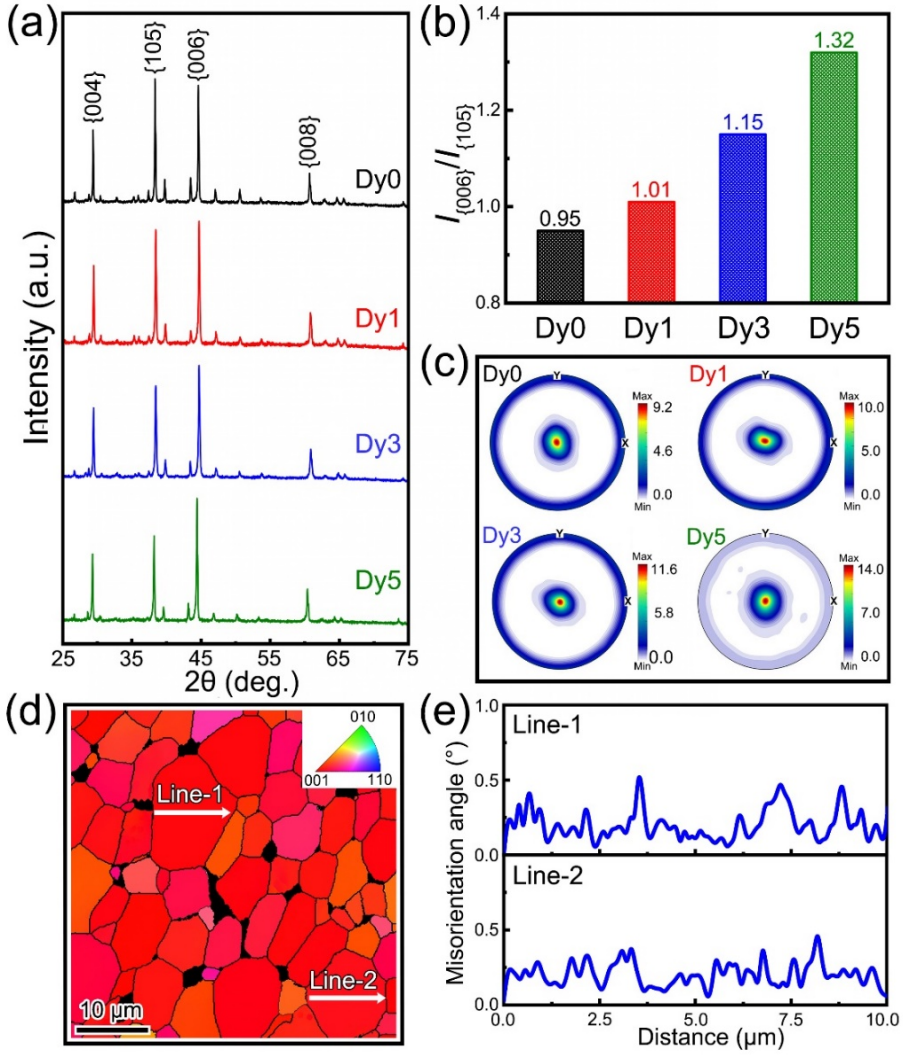

FIGURE 7. Texture analysis of the post-sinter annealed Dy0, MMP Dy1, Dy3, and Dy5

magnets. (a) X-ray diffraction (XRD) patterns. (b) Corresponding values for the peak intensity ratio of the {006} plane to the {105} planes in (a). (c) Corresponding {006} pole figures. The unit is multiples of a random density (MRD). (d) Inverse pole figure (IPF)–Z of the $RE_2Fe_{14}B$ grains in the post-sinter annealed MMP Dy3 magnet. The color represents the crystallographic orientation of the $RE_2Fe_{14}B$ grains. The color code is shown in the standard triangle (inset). (e) Plots of the misorientation angle between the *c* axis of the $RE_2Fe_{14}B$ grains and the normal direction (Z) versus the distance recorded in (d).

3.3.2. Nanoscale characterisation

TEM and STEM–EDXS experiments were conducted to investigate the structures of the constituent phases and elemental distribution in the post-sinter annealed Dy0 and MMP Dy3 magnets. A particular focus was on the microstructural origins of the relatively higher $\mu_0 H_c$ value recorded with little diminishment in the $\mu_0 M_r$ value of the post-sinter annealed MMP Dy3 magnet over the Dy0 one.

Fig. 8a provides a bright field image (BFI) of the post-sinter annealed MMP Dy3 magnet. The red dashed rectangle highlights three $RE_2Fe_{14}B$ grains (G1, G2, and G3) and a RE-rich TJ1. **Figs. 8**b-d display the selective area electron diffraction (SAED) patterns recorded from the <110> zone axis of G1, the <010> zone axis of G2, and the <110> zone axis of the cubic RE-rich TJ1 ($Ia\bar{3}$, a = 1.108 nm). **Fig. 8**e shows the enlarged BFI of the red dashed rectangle shown in **Fig. 8**a. The corresponding STEM–EDXS map of Dy (**Fig. 8**e1) demonstrates the presence of the Dy-lean core–Dy-rich shell microstructure in G1 and G2. The Dy concentrations of the Dy-rich shell and Dy-lean core were measured as ~1.2 at.% and ~0.2 at.%, respectively (**Fig. 8**e2). **Figs. 8**f-f4 reveal the formation of the ZrB_2 phase at the G1/TJ1 interface. Most importantly, an intergranular GB phase was observed with a thickness of ~14 nm between G1 and G3 (**Fig. 8**g). From the corresponding STEM–EDXS maps and line-scan results (**Figs. 8**g1-g4), this thin GB phase was depleted in Fe (yellow) and enriched in Nd (blue), suggesting that it is a non-ferromagnetic low-Fe RE-rich phase.

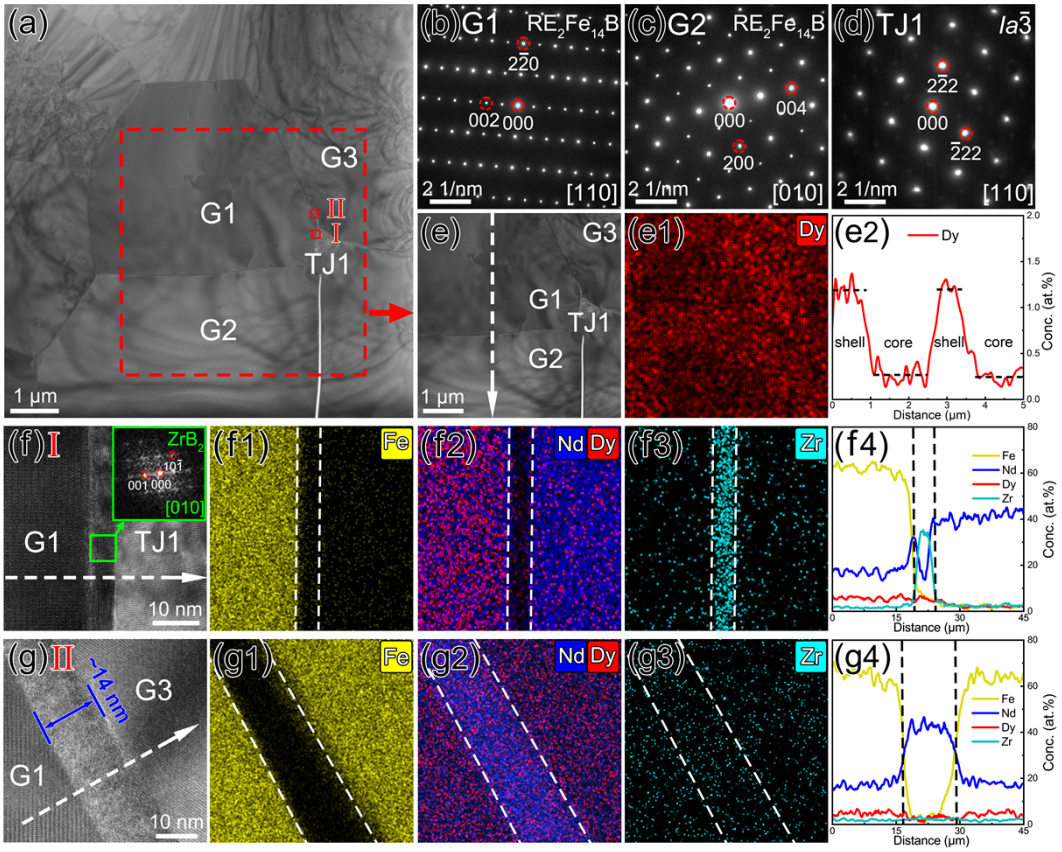

FIGURE 8. TEM and STEM–EDXS analysis of the post-sinter annealed MMP Dy3 magnet. (a) Bright field image (BFI). Selected area electron diffraction (SAED) patterns for the (b) $RE_2Fe_{14}B$ grain G1, (c) G2, and (d) TJ1, respectively. (e) An enlarged view of the red dashed square highlighted in (a). (e1) The elemental distribution of Dy and (e2) the concentration profiles of Dy along the arrow shown in (e). (f) High-resolution transmission electron microscopy (HRTEM) image of the region I shown in (a) indicating the G1/TJ1 interface. The corresponding elemental distribution of (f1) Fe, (f2) Nd + Dy, (f3) Zr, and (f4) line-scan profiles along the arrow in (f). (g) HRTEM image of the region II shown in (a) indicating a low-Fe RE-rich GB phase between G1 and G3. The corresponding elemental distribution of (g1) Fe, (g2) Nd + Dy, (g3) Zr, and (g4) line-scan profiles along the arrow in (g).

Fig. 9a showcases a BFI of the post-sinter annealed Dy0 magnet, indicating three $RE_2Fe_{14}B$ grains (G4, G5, and G6) and a RE-rich TJ2. **Figs. 9**b-c display the SAED patterns recorded from the <010> zone axis of G4 and the <110> zone axis of G5. **Figs. 9**d-e present a high-resolution transmission electron microscopy (HRTEM) image of the TJ2 phase and

corresponding fast Fourier transform (FFT) pattern with the indexing of the $Ia\bar{3}$ structure (a = 1.108 nm). **Figs. 9**f-f4 reveal the formation of the ZrB_2 phase at the G4/G5 GB, which was also observed in the post-sinter annealed MMP Dy3 magnet. An intergranular GB phase was also observed with a thickness of ~10 nm between G5 and G6 (**Fig. 9**g). However, from the corresponding STEM–EDXS maps and line-scan results (**Figs. 9**g-g4), this thin GB phase possessed a much higher Fe concentration of ~50 at.% compared with the one observed in the post-sinter annealed Dy3 magnet, indicating that this high-Fe RE-rich GB phase is ferromagnetic.

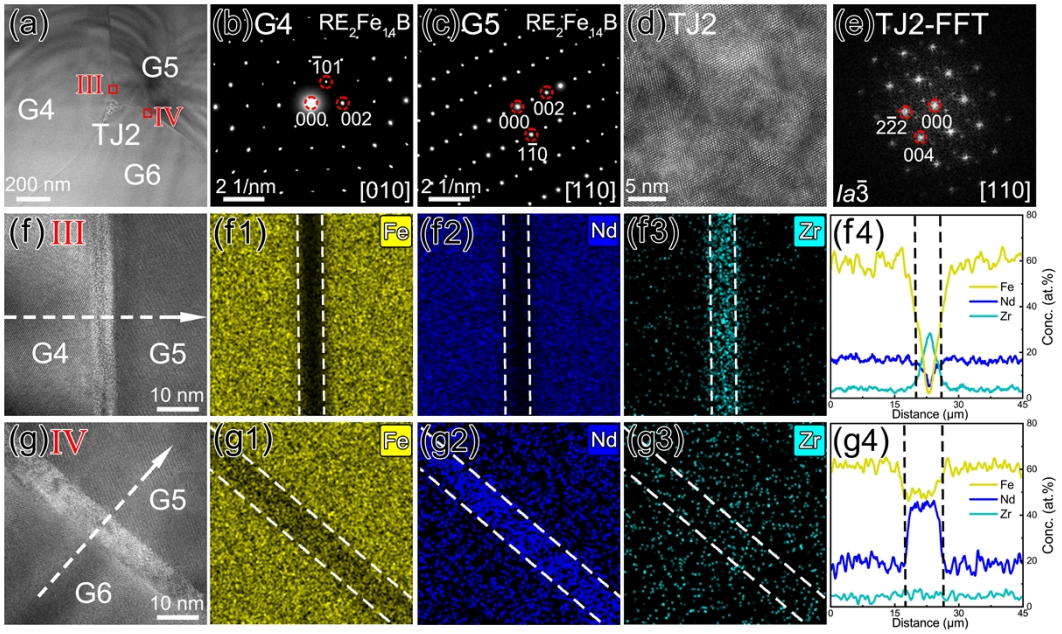

FIGURE 9. TEM and STEM–EDXS analysis of the post-sinter annealed Dy0 magnet. (a) BFI. SAED patterns for the $RE_2Fe_{14}B$ grains (b) G4 and (c) G5. (d) HRTEM image and (e) corresponding FFT result of the TJ2 region. (f) HRTEM image of the region III shown in (a) indicating a ZrB_2 GB phase. The corresponding elemental distribution of (f1) Fe, (f2) Nd, (f3) Zr, and (f4) line-scan profiles along the arrow in (f). (g) HRTEM image of the region IV shown in (a) indicating a high-Fe RE-rich GB phase. The corresponding elemental distribution of (g1) Fe, (g2) Nd, (g3) Zr, and (g4) line-scan profiles along the arrow in (g).

3.3.3. Atomic-scale characterisation

Atomic-scale APT experiments were further conducted to accurately probe the

composition of the intergranular GB phases and the elemental distribution near the $RE_2Fe_{14}B$ grain surface in the post-sinter annealed Dy0 and MMP Dy3 magnets. In the post-sintered annealed MMP Dy3 magnet, two types of the intergranular GB phases were observed (**Figs. 10**a-b). One is the low-Fe RE-rich phase, which consisted exclusively of the light RE elements, i.e., ~60 at.% Nd and ~35 at.% Pr. The Fe concentration was measured to be ~0.1 at.%. The other type of the intergranular GB phase was comprised principally of the Zr and B species, i.e., ~50 at.% B and ~40 at.% Zr. A careful literature review on the Nd–Fe–B–Zr alloys led us to the interpretation that the observed GB phase was likely to be the ZrB_2 phase ($P6_3/mmc$, a = 0.32 nm, c = 0.35 nm) [77], being consistent with the TEM analysis (**Fig. 8**f). Apparently, most of the intergranular GB phase were found to be the RE-rich phase, while the ZrB_2 phase is the minority one (refer to the BSE images in **Fig. 4**).

Two types of the intergranular GB phases were also observed in the post-sinter annealed Dy0 magnet using APT (**Figs. 10**c-d). One is the intergranular ZrB_2 phase, similar to the one observed in the post-sinter annealed MMP Dy3 magnet. However, the other one only possessed a slight enrichment of Nd (~14 at.%) and Pr (~5 at.%), but was significantly enriched in Fe. The Fe concentration was measured to be as high as ~78.4 at.% in this high-Fe RE-rich phase, in consistence with the TEM observation in **Figs. 9**g-g4.

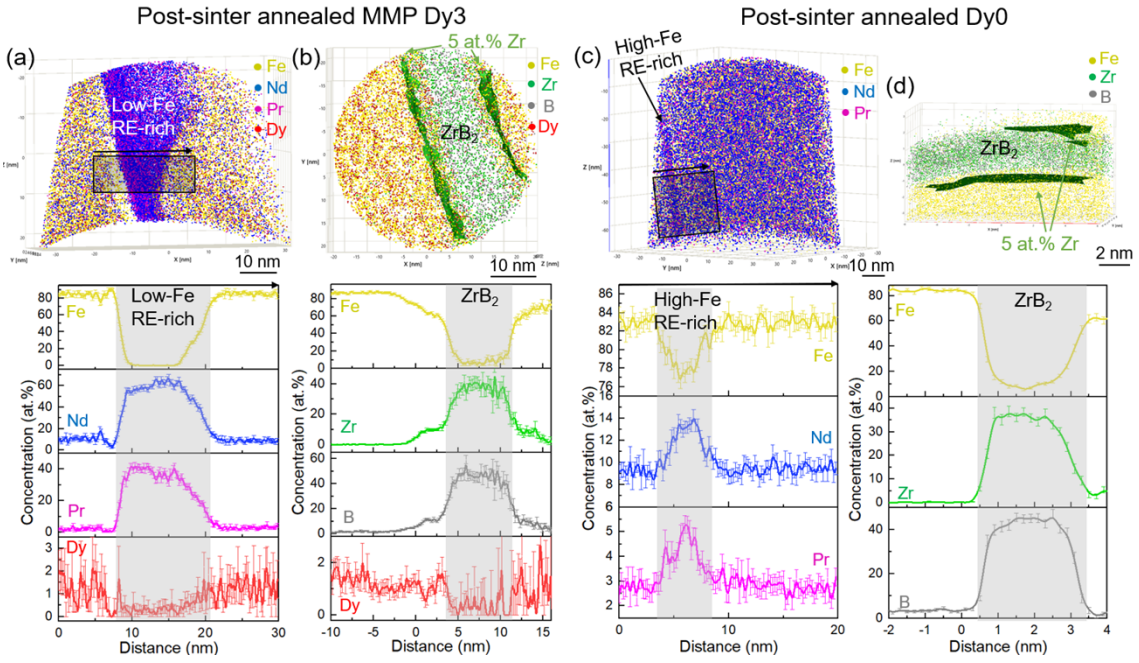

FIGURE 10. Atom probe tomography analysis (APT) of intergranular grain boundary (GB) phases in the post-sinter annealed Dy0 and MMP Dy3 magnets. (a) Atom maps of the Fe, Nd, Pr, Dy for a low-Fe RE-rich phase captured in the MMP Dy3 magnet, and the corresponding 1D concentration profiles along the black arrow. (b) Atom maps of the Fe, Zr, B, Dy for a ZrB_2 phase captured in the MMP Dy3 magnet, and the corresponding proximity histogram based on the 5 at.% Zr iso-concentration surfaces. (c) Atom maps of a high-Fe RE-rich phase captured in the Dy0 magnet, and the corresponding 1D concentration profiles along the black arrow. (d) ZrB_2 phase . (d) Atom maps of a ZrB_2 phase captured in the Dy0 magnet, and the corresponding proximity histogram based on the 5 at.% Zr iso-concentration surfaces.

Fig. 11 presents the elemental distribution, particularly Dy, at the $RE_2Fe_{14}B$ grain surface (shell region) adjacent to the RE-rich phase in the post-sinter annealed Dy0, MMP Dy3 and Dy5 magnets. Five regions of interest (ROIs 1–5) were selected (**Fig. S7**), with the corresponding atom distribution maps of the raw APT datasets shown in **Figs. S8-16**. The derived atomic concentrations of Dy, Fe, B, Nd, Pr, Co, and other species (Cu, Ga, Al, and Si), as well as the Dy/total rare earth (TRE) ratio are summarised in **Table 2**. The Dy/TRE ratio were measured to be 0%, ~11.2%, and 16.6% at the grain surface for the post-sinter annealed Dy0 ROI 1, MMP Dy3 ROI 3, and Dy5 ROI5 regions, respectively. Furthermore, the Dy concentration of the $RE_2Fe_{14}B$ grain surface remained at a similar level for the post-sinter annealed MMP Dy3 magnet. For example, ROIs 2 and 3 from the post-sinter annealed MMP Dy3 magnet possessed a similar Dy/TRE ratio of 11.5% and 11.2%, respectively. When approaching ~3 μm away from the RE-rich phase, the Dy/TRE ratio was reduced to 10.4% (ROI 4).

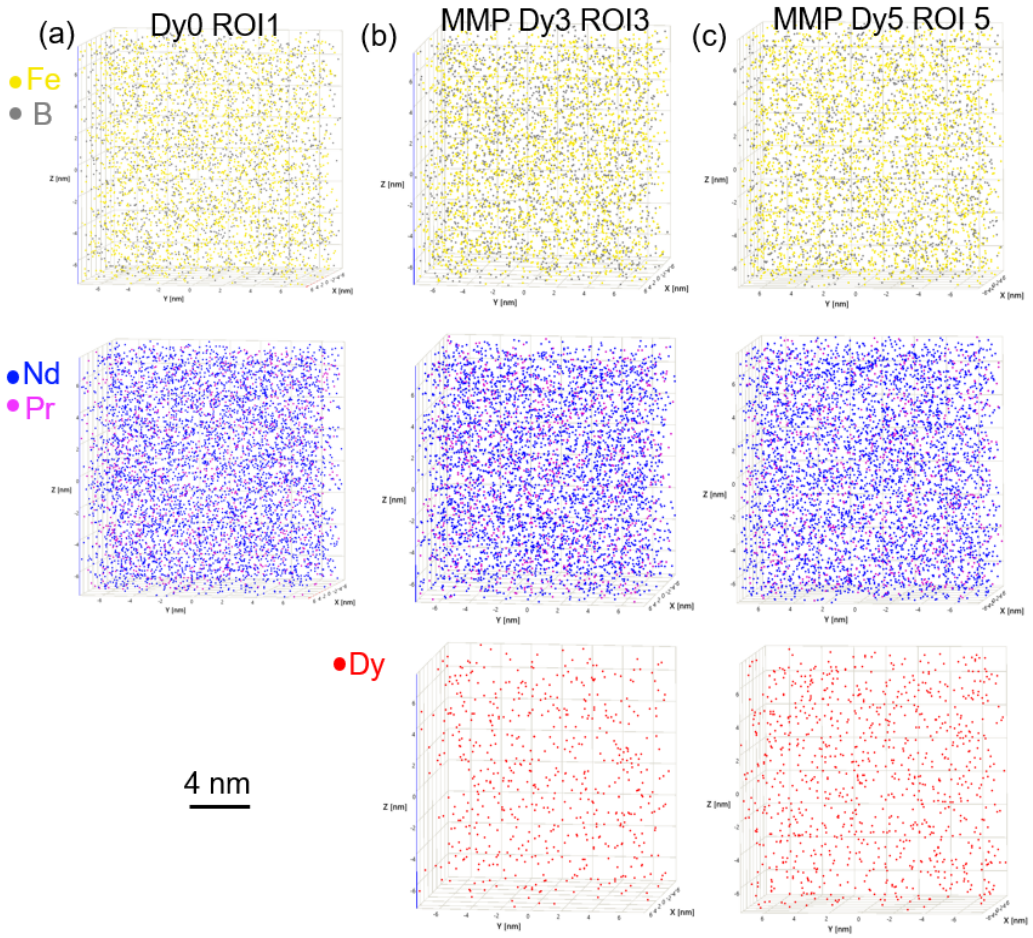

FIGURE 11. Atom distribution maps of the Fe, B, Nd, Pr, and Dy of the $RE_2Fe_{14}B$ grain surface adjacent to the RE-rich phase in the post-sinter annealed (a) Dy0, (b) MMP Dy3, and (c) MMP Dy5 magnets. The dimensions are 15 × 15 × 15 nm^3.

TABLE 2. Atomic concentrations of the Dy, Fe, B, Nd, Pr, Co, and other species, as well as the Dy/TRE ratio of the ROIs 1–5 in the post-sinter annealed Dy0, MMP Dy3, and MMP Dy5 magnets.

Magnets	ROI	Location	Dy	Fe	B	Nd	Pr	Co	Others (Cu, Ga, Al, Si)	Dy/TRE
Dy0	1	grain surface	0	83.08 ±0.31	3.84 ±0.05	9.31 ±0.08	2.76 ±0.04	0.59 ±0.02	0.42 ±0.03	0
Dy3	2	grain surface	1.39 ±0.09	83.55 ±0.92	3.35 ±0.14	8.30 ±0.22	2.43 ±0.12	0.69 ±0.06	0.29 ±0.08	11.5%

Dy3	3	grain surface	1.35 ±0.03	82.60 ±0.32	4.46 ±0.06	8.14 ±0.08	2.52 ±0.04	0.61 ±0.02	0.32 ±0.03	11.2%
Dy3	4	~3 μm away from the grain surface	1.25 ±0.03	82.61 ±0.29	4.43 ±0.05	8.55 ±0.07	2.13 ±0.03	0.62 ±0.02	0.41 ±0.03	10.4%
Dy5	5	grain surface	1.98 ±0.04	83.37 ±0.31	3.57 ±0.05	7.86 ±0.07	2.10 ±0.04	0.69 ±0.02	0.43 ±0.03	16.6%

3.4. Micromagnetic simulations

A model with dimensions of 250×250×250 nm^3 was built and comprised of 125 core–shell $RE_2Fe_{14}B$ grains separated by 5-nm-thick GB phases (**Fig. 12**). The thicknesses of the $(Nd_{1-x}Dy_x)_2Fe_{14}B$ shells was set as 15 nm in our model. The experimental ratio between the thicknesses of the $(Nd_{1-x}Dy_x)_2Fe_{14}B$ shells (~1 μm) and the average size of the $RE_2Fe_{14}B$ grains (~4.1 μm for the post-sinter annealed Dy0 magnet) was ~0.24. The average size of the $RE_2Fe_{14}B$ grains was set as $2 \times \sqrt[3]{\frac{(250 \times 250 \times 250)}{125} \times \frac{3}{4\pi}} = 62$ nm in the model. Therefore, the shell thicknesses were set as 0.24 × 62 = 15 nm in the model (**Fig. 11**).

The simulated demagnetisation curves for the post-sinter annealed Dy0 and MMP Dy1, Dy3, and Dy5 models are provided in **Fig. 12**. The $\mu_0 H_c$ value was increased from 5.22 to 5.55 T with the increasing Dy level from 0 to 1 wt.%. The increment level of the $\mu_0 H_c$ value was ~0.20 T with the increasing Dy level from 1 to 3 wt.%. With the further Dy addition of the same level (from 3 to 5 wt.%), only ~0.07 T enhancement of the $\mu_0 H_c$ value was achieved. Since the Dy-lean core–Dy-rich shell microstructure is absent in the post-sinter annealed MMP Dy 5 magnet, this unique core–shell microstructure is more effective than a uniform $RE_2Fe_{14}B$ grain microstructure in enhancing the $\mu_0 H_c$ value. These micromagnetic simulation results are consistent with the experimental measurements (**Fig. 1**b).

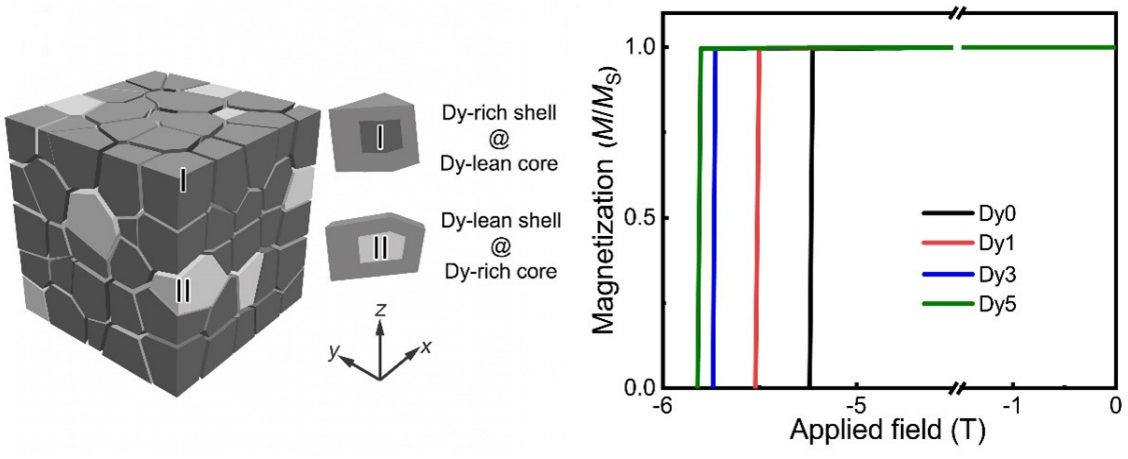

FIGURE 12. A model used for the micromagnetic simulations and the simulated demagnetisation curves of the post-sinter annealed Dy0, MMP Dy1, Dy3, and Dy5 models.

4. Discussion

4.1. The formation and the absence of the core–shell microstructures

Fig. 13 sets out the phenomenology of the formation and absence of the core–shell microstructures in the as-sintered and post-sinter annealed MMP Dy1–Dy5 magnets. The formation of the core–shell microstructures in materials science are not uncommon and almost always reflects a competitive diffusion process between species with disparate diffusion rates (e.g., [78,79]). In this work, the solid-state-diffusion and solution reprecipitation during liquid-phase sintering afforded an opportunity to form the core–shell microstructures in the as-sintered MMP Dy1 and Dy3 magnets (in the low-Dy-level regime), but not the as-sintered MMP Dy5 magnet (in the high-Dy-level regime).

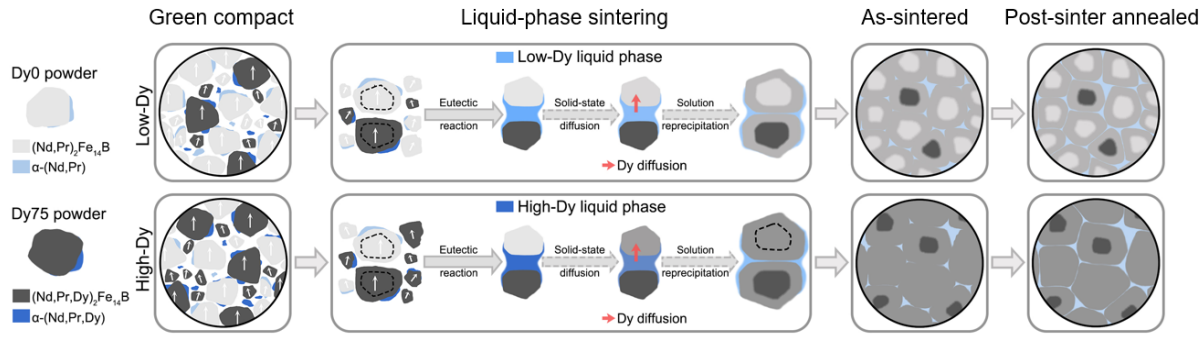

FIGURE 13. Schematics of the microstructural evolution of the MMP Dy1–Dy5 magnets at

the low-Dy-level and high-Dy-level regimes, during green compact, liquid-phase sintering, and at the as-sintered and post-sinter annealed states.

In the step of green compact, the mixtures of the Dy0 and Dy75 powders were aligned in a magnetic field and compacted. The Dy0 powder consisted of a single $(Nd,Pr)_2Fe_{14}B$ grain with a surrounding α-(Nd,Pr) phase. The Dy75 powder was comprised of a single $(Nd,Pr,Dy)_2Fe_{14}B$ grain and an α-(Nd,Pr,Dy)-rich phase. Above the eutectic temperature for the Nd/Pr/Dy–Fe–B systems, the α-(Nd,Pr) phase, α-(Nd,Pr,Dy)-rich phase, and local high-energy regions [80] in the $(Nd,Pr)_2Fe_{14}B$ and $(Nd,Pr,Dy)_2Fe_{14}B$ grains (e.g., asperities) melted together and formed into the RE-rich liquid phase.

Next, at the beginning of liquid-phase sintering for the MMP Dy1–Dy5 magnets magnets, driven by the Dy concentration gradient, the Dy atoms diffused from the RE-rich liquid phase into the interior of the $(Nd,Pr)_2Fe_{14}B$ grain inherited from the Dy0 powders. Though the diffusion source is the RE-rich liquid phase, the diffusion channel within the lattice of the $(Nd,Pr)_2Fe_{14}B$ grain is solid. Therefore, this process is referred to as solid-state-diffusion. Note that the $(Nd,Pr)_2Fe_{14}B$ grain inherited from the Dy0 powders were therefore transformed into the solid-state-diffused $(Nd,Pr,Dy)_2Fe_{14}B$ grain.

The sintering time of 3 h was far enough for the Dy atoms to diffuse within the entire $(Nd,Pr)_2Fe_{14}B$ grain inherited from the Dy0 powders. From Fick's first law, the diffusive flux of Dy (J_{Dy}) can be written as: $J^{Dy} = D^{Dy}\left|\frac{\partial C^{Dy}}{\partial x}\right|$, where C_{Dy} is the concentration of Dy, x is the distance, and D_{Dy} is the diffusion coefficient of Dy. The D_{Dy} value is 2.9×10^{-4} $\mu m^2/s$ at a temperature of 1050 °C in the $Nd_2Fe_{14}B$ phase [81]. The average size of the Dy0 powders was ~3.3 μm. Thus, the time required for the Dy atoms to diffuse through the entire $(Nd,Pr)_2Fe_{14}B$ grain was estimated around $(3.3/2)^2/6D_{Dy} = 1565$ s = 0.4 h [82]. With the increasing Dy75 mass ratio of the mixed powders, the higher Dy concentrations of the RE-rich phase yields a higher value of J_{Dy}. The Dy concentrations of the solid-state-diffused $(Nd,Pr,Dy)_2Fe_{14}B$ grains were increased correspondingly.

Then the RE (Nd, Pr, and Dy) alongside Fe and B atoms initiated to combine and

reprecipitate the $RE_2Fe_{14}B$ phase, growing on top of the solid-state-diffused $(Nd,Pr,Dy)_2Fe_{14}B$ grains. This process is referred to as solution reprecipitation (**Figs. 7d-e**). It was found that the concentrations of the $RE_2Fe_{14}B$ grain surface adjacent to the RE-rich phase remained at a similar level for the post-sinter annealed MMP Dy3 magnet (see the respective Dy/TRE ratio of 11.5% and 11.2% for ROIs 2 and 3, in **Table 2**). This suggests that the reprecipitated $RE_2Fe_{14}B$ phase possessed a fixed Dy/TRE ratio. Furthermore, with the increasing Dy75 mass ratio of the mixed powders, the higher Dy concentrations of the RE-rich phase yields a higher Dy/TRE ratio in the reprecipitated $RE_2Fe_{14}B$ phase (**Table 2**).

During solution reprecipitation, it is assured that the former solid-state diffusion process was retarded since the solid-state-diffused $(Nd,Pr,Dy)_2Fe_{14}B$ grain was no longer contacted with the RE-rich liquid phase. However, concurrent with solution reprecipitation, another type of the solid-state-diffusion initiated from the reprecipitated $RE_2Fe_{14}B$ phase to the solid-state-diffused $(Nd,Pr,Dy)_2Fe_{14}B$ grain. From the APT results (**Table 2**), when approaching 3 μm away from the RE-rich phase, the Dy/TRE ratio was reduced from 11.2% to 10.4%. This suggests the occurrence of the solid-state-diffusion between the reprecipitated $RE_2Fe_{14}B$ phase and the solid-state diffused $RE_2Fe_{14}B$ grain. However, this solid-state-diffusion during solution reprecipitation was overshadowed since its kinetics was much slower than the former one from the RE-rich liquid phase to the $(Nd,Pr)_2Fe_{14}B$ grains inherited from the Dy0 powders.

The post-sinter annealed MMP Dy3 magnet was additionally heated at 1075 ℃ for the durations of 6 and 12 hours. This was intended to examine if the solid-state-diffusion from the reprecipitated $RE_2Fe_{14}B$ phase (Dy-rich shell) to the the solid-state diffused $RE_2Fe_{14}B$ grain (Dy-lean core) led to the absence of the Dy-lean core–Dy-rich shell microstructure. The consequence was that, even after 12 hours of heating, the Dy-lean core–Dy-rich shell microstructure was still preserved (refer to **Fig. 14**), though the concentration difference ΔC was reduced to 1.9 wt.%, compared to the value of 2.6 wt.% after 6 h heat treatment and 3.4 wt.% without any heat treatment (**Table 3**). This finding demonstrates that the diffusion between the Dy-rich shells and the Dy-lean cores cannot fully account for the absence of the Dy-lean core–Dy-rich shell microstructure.

The former solid-state diffusion from the RE-rich liquid phase to the $(Nd,Pr)_2Fe_{14}B$ grains inherited from the Dy0 powders prior to solution reprecipitation is a key factor to account for the absence of the Dy-lean core–Dy-rich shell microstructure in the high-Dy-level regime. In the low-Dy-level regime, the Dy0 mass ratios of the mixed powders were 95.63% and 86.89% for the as-sintered MMP Dy1 and Dy3 magnets. It was therefore more common to observe the reprecipitated $RE_2Fe_{14}B$ phases (Dy-rich shells) on the solid-state-diffused $(Nd,Pr,Dy)_2Fe_{14}B$ grains (Dy-lean cores). In the high-Dy-level regime, the Dy concentrations of the reprecipitated $RE_2Fe_{14}B$ phases were still increased and reached at a similar value (Dy/TRE ratio value of 16.6%) as that of the solid-state-diffused $(Nd,Pr,Dy)_2Fe_{14}B$ grains in the as-sintered MMP Dy5 magnet due to a high diffusion rate. Therefore, the Dy-lean core–Dy-rich shell microstructure diminished.

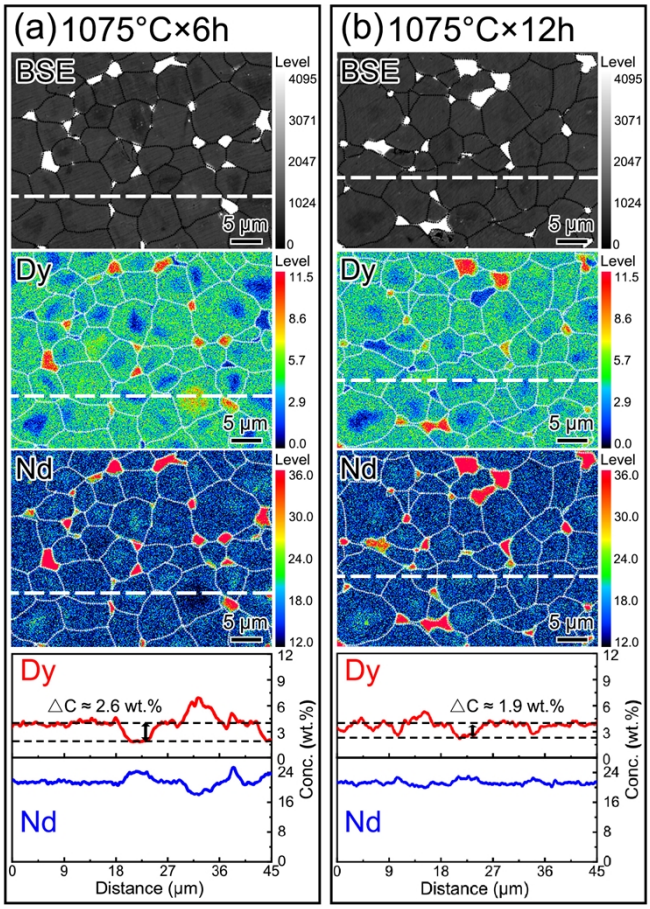

FIGURE 14. BSE image, EPMA maps, and plots of the WDXS line-scans recorded from the post-sinter annealed MMP Dy3 magnets re-sintered at 1075 °C for (a) 6 h, and (b) 12 h.

Table 3. The Dy concentrations measured at the Dy-rich shells and the Dy-lean cores by EPMA for the post-sinter annealed MMP Dy3 magnet without and with additional heat treatment at 1075 ℃ for 6 h and 12 h, respectively. The difference in the Dy concentration between the Dy-rich shells and the Dy-lean cores (ΔC) is also listed.

Condition	Dy concentration of the Dy-rich shells (wt.%)	Dy concentration of the Dy-lean cores (wt.%)	ΔC (wt.%)
Without additional heat treatment	4.4	1.0	3.4
With additional heat treatment at 1075 °C for 6 h	4.3	1.7	2.6
With additional heat treatment at 1075 °C for 12 h	4.1	2.2	1.9

By contrast, at the beginning of liquid-phase sintering for the Dy0 magnet, there was no Dy concentration gradient between the $(Nd,Pr)_2Fe_{14}B$ grain inherited from the Dy0 powders and the RE-rich liquid phase. Therefore, there was no solid-state-diffusion for the Dy species from the RE-rich liquid phase to the $(Nd,Pr)_2Fe_{14}B$ grain. Next, the RE (Nd and Pr), Fe and B atoms still initiated to combine and reprecipitate the $RE_2Fe_{14}B$ phase, growing on top of the the solid-state-diffused $(Nd,Pr,Dy)_2Fe_{14}B$ grains. However, during solution reprecipitation, there was also no diffusion of the Dy species since there was no Dy concentration gradient between the reprecipitate $RE_2Fe_{14}B$ phase and the solid-state-diffused $(Nd,Pr)_2Fe_{14}B$ grain.

Solution reprecipitation was accompanied by the $RE_2Fe_{14}B$ grain growth. Here, the average size of the $RE_2Fe_{14}B$ grains was enlarged from 3.3 to 5.1–8.2 μm in the as-sintered MMP Dy1, Dy3 and Dy5 magnets (**Fig. S17**). The growth rate of the $RE_2Fe_{14}B$ grains increases with the higher volume fraction of the RE-rich liquid phase. Compared to the Dy0 powders, the Dy75 powders possessed a relatively higher fraction of the RE-rich phase (**Table S1**), which may be attributed to the formation of the Dy_2Fe_{17} primary phase upon cooling [83,84]. Therefore, during liquid-phase sintering, the increasing fraction of the Dy75 powders led to a higher volume fraction of the RE-rich liquid phase. This resulted in an increase in the growth rate of $RE_2Fe_{14}B$ grains in the as-sintered MMP magnets processed from the powder mixture

containing a higher fraction of the Dy75 powders. Thus, the grain size of the as-sintered MMP Dy5 magnet is much larger than that of the as-sintered MMP Dy1 and Dy3 magnets. Note that the post-sinter annealing process did not trigger the $RE_2Fe_{14}B$ grain growth based on our experimental results (**Fig. S17, Table S7**).

Below the eutectic temperature for the Nd/Pr/Dy–Fe–B systems during liquid-phase sintering, the α-(Nd,Pr) phase was primarily formed between the neighboring reprecipitated $RE_2Fe_{14}B$ phases. In the step of post-sinter annealing (**Fig. 13**), the α-(Nd,Pr) phase melted again upon heating and then penetrated into the interfaces between the neighboring reprecipitated $RE_2Fe_{14}B$ phases by the capillary action to form uniform RE-rich GBs (**Figs. 4** and **8**). Previous APT results revealed a uniform Dy distribution across thin GB phase in both sintered and GBDP Nd–Dy–Fe–B magnets [11,63]. However, we reported a significant depletion of the Dy species at the RE-rich and ZrB_2 GB phases compared with the $RE_2Fe_{14}B$ grains in the post-sinter annealed MMP Dy3 magnet (**Fig. 10**a). This suggests that the Dy species prefer entering the $RE_2Fe_{14}B$ phase than the Nd-rich phase, in excellent agreement with previous DFT calculation results [85]. The temperatures for two-step post-sinter annealing of 890 and 490 °C were lower than that for liquid-phase sintering of 1075 °C. The elemental diffusion was relatively limited during post-sinter annealing, which explains the unchanged core–shell microstructures in the post-sinter annealed MMP Dy1, Dy3, and Dy5 magnets compared with the as-sintered ones (**Fig. 4**).

4.2. Correlation between the Dy-lean core–Dy-rich shell microstructure and magnetic properties

The Dy-lean core–Dy-rich shell microstructure plays a significant role in a high synergy of $\mu_0 H_c$ and $\mu_0 M_r$ of the post-sinter annealed MMP Nd–Dy–Fe–B magnets (**Figs. 1**, **2** and **12**, **Table 1**). This is significant in the context of the MMP Nd–Dy–Fe–B magnets being applied to large-scale production. The $\mu_0 H_c$ of a sintered Nd–Fe–B magnet can be analysed using the Kronmüller equation [86]:

$$\mu_0 H^c = \mu^0 H^N = \alpha(\mu^0 H^A) - N^{eff}(\mu^0 M^s) \quad (1)$$

where $\mu_0 H_N$ correspond to the nucleation field of the $Nd_2Fe_{14}B$ phase. α and N_{eff} are microstructural parameters and local effective demagnetising factor. Generally, the demagnetisation process begins with the nucleation of the reversed domains that occur preferentially at the outer regions in the $Nd_2Fe_{14}B$ grains near the RE-rich TJs or GBs. The $\mu_0 H_A$ value of the $(Nd_{1-x}Dy_x)_2Fe_{14}B$ increases with the increasing value of x [87]. The $\mu_0 H_A$ values of the Dy-rich shells were therefore higher in the post-sinter annealed MMP Dy3 magnet than the Dy0 and Dy1 ones. The $\mu_0 H_c$ value of the post-sinter annealed MMP Nd–Dy–Fe–B magnet was therefore increased with the increasing Dy level from 0 to 3 wt.%. This is evidenced by the higher demagnetising field required for the nucleation of the reversed domains in the post-sinter annealed MMP Dy3 magnet than the Dy0 and Dy1 ones (**Fig. 3**).

The ZrB_2 phase, being observed in both the post-sinter annealed Dy0 and MMP Dy3 magnets, was ruled out as a factor contributing to the relatively high coercivity in the post-sinter annealed MMP Dy3 magnet compared with the Dy0 one. Most importantly, the intergranular RE-rich GB phase showcased contrasting Fe concentrations, which are ~78.4 at.% and ~0.1 at.% for the post-sinter annealed Dy0 and MMP Dy3 magnets, respectively (see **Figs. 10**a and c). This implies that the magnetism of the RE-rich GB phases is different, which are ferromagnetic and non-ferromagnetic for the post-sinter annealed Dy0 and MMP Dy3 magnets, respectively. The non-ferromagnetic RE-rich GB phase is believed to weaken the ferromagnetic coupling between adjacent Dy-rich shells and therefore enhance the α value of the post-sinter annealed MMP Dy3 magnet compared with the Dy0 one. Another effect for the non-ferromagnetic RE-rich GB phase is that some $RE_2Fe_{14}B$ grains were therefore exchange-decoupled. Then the reversed domains cannot penetrate through these non-ferromagnetic GB phases during demagnetisation. Consequently, these $RE_2Fe_{14}B$ grains reversed separately and not as expected in a group where the ferromagnetic GB phases were observed (**Fig. 3**).

The $\Delta\mu_0 H_c/\Delta Dy$ value was lowered in the high-Dy-level regime. This was primarily caused by the enlarged average size of the $RE_2Fe_{14}B$ grains from 6.3 to 8.2 μm with the increasing Dy level from 3 to 5 wt.% (**Fig. 6**), though the formation of the agglomerated ZrB_2 platelets within large intergranular Nd-rich phases may inhibit grain growth [77]. The

coercivity was inversely proportional to the natural logarithm of the $RE_2Fe_{14}B$ grain size D, following the relation: $\mu_0 H_c = a - b\ln D^2$ [7]. Although the Dy-lean core–Dy-rich shell microstructure diminished, the local $\mu_0 H_A$ values of the outer regions in the $RE_2Fe_{14}B$ grains were still increased with the increasing Dy level from 3 to 5 wt.% (**Fig. 5**c). But the enlarged average size of the $RE_2Fe_{14}B$ grains posed a more negative effect than the increase of the local $\mu_0 H_A$ value on the enhancement of $\mu_0 H_c$ simultaneously.

The increasing Dy level led to the unavoidable reduction of the intrinsic $\mu_0 M_s$ of the $RE_2Fe_{14}B$ grains, and therefore lowering the $\mu_0 M_r$ values of the post-sinter annealed MMP Dy1–Dy5 magnets. The reduction of the $\Delta\mu_0 M_r/\Delta$Dy value was further increased in the high-Dy-level regime (Fig. 1). This was primarily caused by the formation of the solid-state-diffused $(Nd,Pr,Dy)_2Fe_{14}B$ grains with high Dy concentrations during liquid-phase sintering. More Dy atoms diffused into the $(Nd,Pr)_2Fe_{14}B$ grains inherited from the Dy0 powders in the post-sinter annealed MMP Dy5 magnet. The Dy concentrations of the solid-state-diffused $(Nd,Pr,Dy)_2Fe_{14}B$ grains were higher in the post-sinter annealed MMP Dy5 magnet than in the Dy1 or Dy3 ones. This enlarged the reduction of the $\Delta\mu_0 M_r/\Delta$Dy value in the post-sinter annealed MMP Dy5 magnet (**Fig. 1**b).

5. Conclusions

We have demonstrated a feasible approach to achieve a uniform Dy-lean core–Dy-rich shell microstructure in the MMP Nd–Dy–Fe–B magnets. Major conclusions are as follows:

(1) By sweeping a range of mix ratios of the Dy75 and Dy0 powders, the post-sinter annealed MMP Dy3 magnet exhibits an excellent coercivity of 2.4 T with little sacrifice in remanent magnetisation and maximum energy product (1.35 T and 43.6 MGOe), high thermal stability ($|\beta|$ = 0.531 %/°C) and squareness factor (>95%), collectively.

(2) In the low-Dy-level regime (Dy level ≤ 3 wt.%), a uniform Dy-lean core–Dy-rich shell microstructure was achieved through solid-state-diffusion and solution reprecipitation during liquid-phase sintering. The Dy-rich shells were found to enhance the nucleation field of the reversed domains within the $RE_2Fe_{14}B$ grains. The non-ferromagnetic low-Fe RE-rich phase is

responsible for decoupling of the neighboring ferromagnetic $RE_2Fe_{14}B$ grains.

(3) In the high-Dy-level regime (Dy level > 3 wt.%), the Dy75 powders broke up the Dy-lean core–Dy-rich shell microstructure, and led to enlarged $RE_2Fe_{14}B$ grains, limiting the coercivity enhancement. Despite the enhanced {001} texture, the drastic degradation of the remanent magnetisation highlights the crucial role of microstructure, where a Dy-lean core–Dy-rich shell is essential to tackle the coercivity-remanent magnetisation trade-off.

To summarise, the two-step formation mechanism of uniform Dy-lean core–Dy-rich shell microstructure was unveiled through multi-scale microstructural characterisation, which may shed light on more efficient utilisation of the heavy RE element Dy in the fabrication of high-performance Nd–Dy–Fe–B magnets.

Acknowledgements

This work was supported by National Key Research and Development Program of China (2021YFB3501504), National Natural Science Foundation of China (U21A2052), Key Research and Development Program of Zhejiang Province (2021C01192), “Leading Goose” R&D Program of Zhejiang Province (2022C01110), and 2022 USYD-ZJU Parternership Collaboration Awards (PCA). The authors thank Dr. Xiangyuang Cui, Dr. Vijay Bhatia, Dr. Takanori Sato and Mr. Jacob Byrnes at the University of Sydney, Prof. Zijian Hong, Associate Prof. Yuhui Huang, Prof. Yongjun Wu at Zhejiang University, and Prof. Tianyu Ma at the Xi'an Jiaotong University for their technical support and discussions. SPR acknowledges partial financial support from the Australian Research Council Discovery Program (DP200100940). The authors acknowledge the facilities, and the scientific and technical assistance of Sydney Microscopy & Microanalysis, which is the University of Sydney's node of Microscopy Australia node.

References

[1] S. Massari, M. Ruberti, Rare earth elements as critical raw materials: Focus on international markets and future strategies, Resour. Policy 38 (2013) 36-43.

[2] X. Tang, H. Sepehri-Amin, A. Bolyachkin, T. Ohkubo, K. Hono, (Nd,La,Ce)-Fe-B hot-deformed magnets for application of variable-magnetic-force motors, Acta Mater. 228 (2022) 117747.

[3] H. Nakamura, The current and future status of rare earth permanent magnets, Scripta Mater. 154 (2018) 273-276.

[4] S. Hirosawa, Preface to the viewpoint set on: permanent magnets and underlining material science, Scripta Mater. 154 (2018) 245-247.

[5] J.M.D. Coey, Perspective and prospects for rare earth permanent magnets, Engineering 6 (2019) 119-131.

[6] J.F. Herbst, $R_2Fe_{14}B$ materials: Intrinsic properties and technological aspects, Rev. Mod. Phys. 63 (1991) 819-898.

[7] K. Hono, H. Sepehri-Amin, Strategy for high-coercivity Nd-Fe-B magnets, Scripta Mater. 67 (2012) 530-535.

[8] O. Gutfleisch, M.A. Willard, E. Brück, C.H. Chen, S.G. Sankar, J.P. Liu, Magnetic materials and devices for the 21st century: stronger, lighter, and more energy efficient, Adv. Mater. 23 (2011) 821-842.

[9] W.F. Li, H. Sepehri-Amin, T. Ohkubo, N. Hase, K. Hono, Distribution of Dy in high-coercivity (Nd,Dy)-Fe-B sintered magnet. Acta Mater. 59 (2011) 3061-3069.

[10] L.Q. Yu, Y.H. Wen, M. Yan, Effects of Dy and Nb on the magnetic properties and corrosion resistance of sintered NdFeB, J. Magn. Magn. Mater. 283 (2004) 353-356.

[11] M. Yamada, H. Kato, H. Yamamoto, Y. Nakagawa, Crystal-field analysis of the magnetization process in a series of $Nd_2Fe_{14}B$-type compounds, Phys. Rev. B 38 (1988) 620.

[12] T.G. Woodcock, Y. Zhang, G. Hrkac, G. Ciuta, N.M. Dempsey, T. Schrefl, D. Givord, Understanding the microstructure and coercivity of high performance NdFeB-based magnets, Scripta Mater. 67 (2012) 536-541.

[13] United States Department of Energy, Critical Materials Strategy. United States Department of Energy, Washington D.C. 190 (2011).

[14] R.L. Moss, E. Tzimas, H. Kara, P. Willis, J. Kooroshy, The potential risks from metals bottlenecks to the deployment of Strategic Energy Technologies, Energ. Policy 55 (2013) 556-564.

[15] S. Hoenderdaal, L.T. Espinoza, F. Marscheider-Weidemann, W. Graus, Can a dysprosium shortage threaten green energy technologies? Energy 49 (2013) 344-355.
[16] A. Filippas, G. Sempros, C. Sarafidis, Critical rare earths: the future of Nd & Dy and prospects of end-of-life product recycling, Mater. Today Proc. 37 (2021) 4058-4063.
[17] M. Honshima, K. Ohashi, High-energy NdFeB magnets and their applications, J. Mater. Eng. Perform. 3 (1994) 218-222.
[18] W.Q. Liu, H. Sun, X.F. Yi, X.C. Liu, D.T. Zhang, M. Yue, J.X. Zhang, Coercivity enhancement in Nd-Fe-B sintered permanent magnet by Dy nanoparticles doping, J. Alloys Compd. 501 (2010) 67-69.
[19] Z.B. Li, Y. Qin, Y. Li, Y.L. Liu, Y.F. Li, X.F. Zhang, Effect of DyH_x addition on the elemental distribution, magnetization reversal and coercivity in sintered Nd–Fe–B magnets, Mater. Res. Express 6 (2019) 126111.
[20] Y.J. Zhang, T.Y. Ma, X.L. Liu, P. Liu, J.Y. Jin, J.D. Zou, M. Yan, Coercivity enhancement of Nd-Fe-B sintered magnets with intergranular adding (Pr, Dy, Cu)−H_x powders, J. Magn. Magn. Mater. 399 (2016) 159-163.
[21] F. Xu, L.T. Zhang, X.P. Dong, Q.Z. Liu, M. Komuro, Effect of DyF_3 additions on the coercivity and grain boundary structure in sintered Nd-Fe-B magnets, Scripta Mater. 64 (2011) 1137-1140.
[22] A.M. Gabay, M. Marinescu, W.F. Li, J.F. Liu, G.C. Hadjipanayis, Dysprosium-saving improvement of coercivity in Nd-Fe-B sintered magnets by Dy_2S_3 additions, J. Appl. Phys. 109 (2011) 083916.
[23] L.P. Liang, T.Y. Ma, P. Zhang, M. Yan, Effects of $Dy_{71.5}Fe_{28.5}$ intergranular addition on the microstructure and the corrosion resistance of Nd-Fe-B sintered magnets, J. Magn. Magn. Mater. 384 (2015) 133-137.
[24] X.L. Liu, X.J. Wang, L.P. Liang, P. Zhang, J.Y. Jin, Y.J. Zhang, T.Y. Ma, M. Yan, Rapid coercivity increment of Nd–Fe–B sintered magnets by $Dy_{69}Ni_{31}$ grain boundary restructuring, J. Magn. Magn. Mater. 370 (2014) 76-80.
[25] B.B. Zhou, X.B. Li, X.L. Liang, G.L. Yan, K. Chen, A.R. Yan, Improvement of the magnetic property, thermal stability and corrosion resistance of the sintered Nd-Fe-B magnets with $Dy_{80}Al_{20}$ addition, J. Magn. Magn. Mater. 429 (2017) 257-262.
[26] X.F. Zhang, S. Guo, C.J. Yan, L.W. Cai, R.J. Chen, D. Lee, A.R. Yan, Improvement of the thermal stability of sintered Nd-Fe-B magnets by intergranular addition of $Dy_{82.3}Co_{17.7}$, J. Appl. Phys. 115 (2014) 17A757.

[27] W.B. Fu, S. Guo, C.W. Lin, R.J. Chen, X.C. Liu, D. Lee, A.R. Yan, Effect of rare-earth content on coercivity and temperature stability of sintered Nd-Fe-B magnets prepared by dual-alloy method, IEEE Trans. Magn. 49 (2013) 3258-3261.
[28] C.W. Lin, S. Guo, W.B. Fu, R.J. Chen, D. Lee, A.R. Yan, Dysprosium diffusion behavior and microstructure modification in sintered Nd-Fe-B magnets via dual-alloy method, IEEE Trans. Magn. 49 (2013) 3233-3236.
[29] A.S. Kim, High coercivity Nd-Fe-B magnets with lower dysprosium content, J. Appl. Phys. 63 (1988) 3519-3521.
[30] X.L. Liu, M.J. Pan, P. Zhang, T.Y. Ma, L.Z. Zhao, L.W. Li, Enhanced magnetic properties in chemically inhomogeneous Nd-Dy-Fe-B sintered magnets by multi-main-phase process, J. Rare Earths 39 (2020) 558-564.
[31] T. Helbig, K. Loewe, S. Sawatzki, M. Yi, B.X. Xu, O. Gutfleisch, Experimental and computational analysis of magnetization reversal in (Nd,Dy)-Fe-B core shell sintered magnets, Acta Mater. 127 (2017) 498-504.
[32] B.X. Peng, T.Y. Ma, Y.J. Zhang, J.Y. Jin, M. Yan, Improved thermal stability of Nd-Ce-Fe-B sintered magnets by Y substitution, Scripta Mater. 131 (2017) 11-14.
[33] B. Gault, M.P. Moody, Julie M. Cairney, S.P. Ringer, Atom Probe Microscopy, Springer Series in Materials Science 160 (2012).
[34] S. Wallis, Binomial Confidence intervals and contingency tests: Mathematical fundamentals and the evaluation of alternative methods. J. Quant. Linguist. 20 (2013) 178-208.
[35] D.J. Larson, T.J. Prosa, R.M. Ulfig, B.P. Geiser, T.F. Kelly, Local electrode atom probe tomography, Springer, New York (2013).
[36] Magpar, Available from: http://www.magpar.net/FrontPage, Accessed date: 31 July 2018.
[37] W. Scholz, J. Fidler, T. Schrefl, D. Suess, H. Forster, V. Tsiantos, Scalable parallel micromagnetic solvers for magnetic nanostructures, Comput. Mater. Sci. 28 (2003) 366-383.
[38] T. Oikawa, H. Yokota, T. Ohkubo, K. Hono, Large-scale micromagnetic simulation of Nd-Fe-B sintered magnets with Dy-rich shell structures, AIP Adv. 6 (2016) 056006.
[39] M. Sagawa, S. Fujimura, H. Yamamoto, Y. Matsuura, and S. Hirosawa, Magnetic properties of rare‐earth‐iron‐boron permanent magnet materials, J. Appl. Phys. 57 (1985) 4094.
[40] S. Hirosawa, Y. Matsuura, H. Yamamoto, S. Fujimura, M. Sagawa, and H. Yamauchi, Magnetization and magnetic anisotropy of $R_2Fe_{14}B$ measured on single crystals, J. Appl. Phys. 59 (1986) 873.

[41] J. Fliegans, C.Rado, R.Soulas, L.Guetaz, O.Tosoni, N.M. Dempsey, G.Delette, Revisiting the demagnetization curves of Dy-diffused Nd-Fe-B sintered magnets, J. Magn. Magn. Mater. 520 (2021) 167280.

[42] L.H. Liu, H. Sepehri-Amin, T. Ohkubo, M. Yano, A. Kato, N. Sakuma, T. Shoji, K. Hono, Coercivity enhancement of hot-deformed Nd-Fe-B magnets by the eutectic grain boundary diffusion process using $Nd_{62}Dy_{20}Al_{18}$ alloy, Scripta Mater. 129 (2017) 44-47.

[43] J. Li, L. Liu, H. Sepehri-Amin, X. Tang, T. Ohkubo, N. Sakuma, T. Shoji, A. Kato, T. Schrefl, K. Hono, Coercivity and its thermal stability of Nd-Fe-B hot-deformed magnets enhanced by the eutectic grain boundary diffusion process, Acta Mater. 161 (2018) 171-181.

[44] H.Y. Liu, G. Wang, Y. Hong, D.C. Zeng, Effect of heat treatment time on Dy-Cu alloy diffusion process in Dy-containing commercial Nd-Fe-B sintered magnets, Acta Metall. Sin. 31 (2018) 496-502.

[45] N. Oono, M. Sagawa, R. Kasada, H. Matsui, A. Kimura, Production of thick high-performance sintered neodymium magnets by grain boundary diffusion treatment with dysprosium-nickel-aluminum alloy, J. Magn. Magn. Mater. 323 (2011) 297-300.

[46] F.G. Chen, T.Q. Zhang, W.H. Zhang, L.T. Zhang, Y.X. Jin, Dependence of the demagnetization behavior on the direction of grain boundary diffusion in sintered Nd-Fe-B magnets, J. Magn. Magn. Mater. 465 (2018) 392-398.

[47] F.G. Chen, L.T. Zhang, Y.X. Jin, Y. Cheng, Simultaneous enhancement of the coercivity and remanence at high temperatures in a sintered Nd-Fe-B magnet after grain boundary diffusion with $Dy_{60}Co_{40}$ alloy, Mater. Charact. 144 (2018) 547-553.

[48] S.W. Zhong, M.N. Yang, S.U. Rehman, Y.J. Lu, J.J. Li, B. Yang, Microstructure, magnetic properties and diffusion mechanism of DyMg co-deposited sintered Nd-Fe-B magnets, J. Alloys Compd. 819 (2020) 153002.

[49] T.H. Kim, S.R. Lee, H.J. Kim, M.W. Lee, T.S. Jang, Simultaneous application of Dy-X (X = F or H) powder doping and dip-coating processes to Nd-Fe-B sintered magnets, Acta Mater. 93 (2015) 95-104.

[50] M. Itakura, M. Namura, M. Nishida, H. Nakamura, Elemental distribution near the grain boundary in a Nd-Fe-B sintered magnet subjected to grain-boundary diffusion with Dy_2O_3, Mater. Trans. 61 (2020) 438-443.

[51] M. Soderžnik, K.Ž. Rožman, S. Kobe, P. McGuiness, The grain-boundary diffusion process in Nd-Fe-B sintered magnets based on the electrophoretic deposition of DyF_3, Intermetallics 23 (2012) 158-162.

[52] X. Yang, S. Guo, G.F. Ding, X.J. Cao, J.L. Zeng, J. Song, A.R. Yan, Improvement of DyF_3 diffusion efficiency in sintered Nd-Fe-B magnets by stack diffusion technology, J. Magn. Magn. Mater. 475 (2019) 754-758.
[53] T.H. Kim, S.R. Lee, S.J. Yun, S.H. Lim, H.J. Kim, M.W. Lee, T.S. Jang, Anisotropic diffusion mechanism in grain boundary diffusion processed Nd-Fe-B sintered magnet, Acta Mater. 112 (2016) 59-66.
[54] W.X. Ji, W.Q. Liu, M. Yue, D.T. Zhang, J.X. Zhang, Coercivity enhancement of recycled Nd-Fe-B sintered magnets by grain boundary diffusion with DyH_3 nano-particles, Phys. B 476 (2015) 147-149.
[55] X.J. Cao, L. Chen, S. Guo, X.B. Li, P.P. Yi, A.R. Yan, G.L. Yan, Coercivity enhancement of sintered Nd-Fe-B magnets by efficiently diffusing DyF_3 based on electrophoretic deposition, J. Alloys Compd. 631 (2015) 315-320.
[56] K.H. Bae, T.H. Kim, S.R. Lee, H.J. Kim, M.W. Lee, T.S. Jang, Magnetic and microstructural characteristics of DyF_3/DyH_x dip-coated Nd-Fe-B sintered magnets, J. Alloys Compd. 612 (2014) 183-188.
[57] J.Y. Kong, T.H. Kim, S.R. Lee, H.J. Kim, M.W. Lee, T.S. Jang, Effect of surface etching on the magnetic properties and grain-boundary Dy-diffusion in DyH_2-dip-coated sintered Nd-Fe-B magnets, Met. Mater. Int. 21 (2015) 600-606.
[58] J.Y. Choi, H.W. Kwon, B.A. Kim, J.G. Lee, Low melting-point diffusion salts of heavy rare-earth for enhancing coercivity of grain-boundary-diffusion-processed Nd-Fe-B-type magnet, J. Magn. 25 (2020) 205-209.
[59] B.H. Wu, X.F. Ding, Q.K. Zhang, L.J. Yang, B.Z. Zheng, F.Q. Hu, Z.L. Song, The dual trend of diffusion of heavy rare earth elements during the grain boundary diffusion process for sintered Nd-Fe-B magnets, Scripta Mater. 148 (2018) 29-32.
[60] Y.J. Cao, P.J. Zhang, G.Q. Xu, Y.H. Liu, J.Q. Liu, Y.C. Wu, J.W. Chen, X.F. Yi, Study on the corrosion resistance of (Nd, Dy)-Fe-B magnets obtained by grain boundary diffusion method, IEEE Trans. Mag. 57 (2021) 1-6.
[61] T.H. Kim, T.T. Sasaki, T. Ohkubo, Y. Takada, A. Kato, Y. Kaneko, K. Hono, Microstructure and coercivity of grain boundary diffusion processed Dy-free and Dy-containing Nd-Fe-B sintered magnets, Acta Mater. 172 (2019) 139-149.
[62] K. Löewe, C. Brombacher, M. Katter, O. Gutfleisch, Temperature-dependent Dy diffusion processes in Nd-Fe-B permanent magnets, Acta Mater. 83 (2015) 248-255.
[63] H. Sepehri-Amin, T. Ohkubo, K. Hono, The mechanism of coercivity enhancement by the

grain boundary diffusion process of Nd-Fe-B sintered magnets, Acta Mater. 61 (2013) 1982-1990.
[64] W.D. Li, Q.K. Zhang, Q.H. Zhu, S. Xiao, C. Xu, L.J. Yang, B.Z. Zheng, S.D. Mao, Z.L. Song, Formation of anti-shell/core structure of heavy rare earth elements (Tb, Dy) in sintered Nd-Fe-B magnet after grain boundary diffusion process, Scripta Mater. 163 (2019) 40-43.
[65] X.H. Cheng, J. Li, L. Zhou, T. Liu, X.J. Yu, B. Li, Influence of Al/Cu content on grain boundary diffusion in Nd-Fe-B magnet via in-situ observation, J. Rare Earths 37 (2019) 398-403.
[66] B.H. Wu, Q.K. Zhang, W.D. Li, X.F. Ding, L.J. Yang, A.G. Wattoo, L.J. Zhang, S.D. Mao, Z.L. Song, Grain boundary diffusion of magnetron sputter coated heavy rare earth elements in sintered Nd-Fe-B magnet, J. Appl. Phys. 123 (2018) 245112.
[67] R.M. Wang, A.Z. Sun, H.Z. Lang, X.T. Tang, Dy Electrodeposition on Sintered Nd-Fe-B, IEEE Mag. Lett. 10 (2019) 1-5.
[68] S.Q. Hu, K. Peng, H. Chen, Influence of annealing temperature on the Dy diffusion process in NdFeB magnets, J. Magn. Magn. Mater. 426 (2017) 340-346.
[69] S. Fu, M. Yan, J.Y. Jin, H. Nagata, J.H. Xie, Further enhancing the coercivity of Nd-Tb-Fe-B sintered magnets by Dy grain boundary diffusion, Mater. Lett. 283 (2021) 128718.
[70] X.D. Fan, G.F. Ding, K. Chen, S. Guo, C.Y. You, R.J. Chen, D. Lee, A.R. Yan, Whole process metallurgical behavior of the high-abundance rare-earth elements LRE(La, Ce, and Y) and the magnetic performance of $Nd_{0.75}LRE_{0.25}$-Fe-B sintered magnets, Acta Mater. 154 (2018) 343-354.
[71] Y.J. Zhang, T.Y. Ma, M. Yan, J.Y. Jin, B. Wu, B.X. Peng, Post-sinter annealing influences on coercivity of multi-main-phase Nd-Ce-Fe-B magnets, Acta Mater. 146 (2017) 97-105.
[72] H. Chen, R. Han, J. Qu, Y. Yao, J. Liu, W. Li, S. P. Ringer, S. Dong, R. Zheng, Atomic scale insights into the segregation/partitioning behaviour in as-sintered multi-main-phase Nd-Ce-Fe-B permanent magnets, J. Alloys Compd. 846 (2020) 156248.
[73] J.Y. Jin, M. Yan, T.Y. Ma, W. Li, Y.S. Liu, Z.H. Zhang, S. Fu, Balancing the microstructure and chemical heterogeneity of multi-main-phase Nd-Ce-La-Fe-B sintered magnets by tailoring the liquid-phase-sintering, Mater. Design 186 (2020) 108308.
[74] J.Y. Jin, M. Yan, Y.S. Liu, B.X. Peng, G.H. Bai, Attaining high magnetic performance in as-sintered multi-main-phase Nd-La-Ce-Fe-B magnets: toward skipping the post-sinter annealing treatment, Acta Mater. 69 (2019) 248-259.
[75] M. Li, R.J. Chen, C.X. Jin, J.H. Yu, X. Tang, G.C. Chen, J. Sun, Z.X. Wang, A.R. Yan,

Texture and microstructure improvement of hot-deformed magnets with platelet-like nano h-BN addition, Scripta Mater. 152 (2018) 127-131.
[76] T.T. Song, X. Tang, W.Z. Yin, J.Y. Ju, Z.X. Wang, Q.B. Liu, Y. Tang, R.J. Chen, A.R. Yan, Magnetic properties improvement of hot-deformed Nd-Fe-B permanent magnets by Pr-Cu eutectic pre-diffusion process, Acta Mater. 174 (2019) 332-341.
[77] M. Matzinger, J. Fidler, A. Fujita, I.R. Harris, Microstructure of solid-HDDR Nd-Fe-B: Zr magnets, J. Magn. Magn. Mater. 157-158 (1996) 54-56.
[78] J.F. Hu, H. Gu, Z.G. Chen, S.H. Tan, D.L. Jiang, M. Rühle, Core-shell structure from the solution-reprecipitation process in hot-pressed AlN-doped SiC ceramics, Acta Mater. 55 (2007) 5666-5673.
[79] L. Liu, X.Y. Cui, J.T. Jiang, B. Zhang, K. Nomoto, L. Zhen, S.P. Ringer, Segregation of the major alloying elements to $Al_3(Sc,Zr)$ precipitates in an Al-Zn-Mg-Cu-Sc-Zr alloy, Mater. Charact. 157 (2019) 109898.
[80] R.M. German, P. Suri, S.J. Park, Review: liquid phase sintering, J. Mater. Sci. 44 (2009) 1-39.
[81] B.A. Cook, J.L. Harringa, F.C. Laabs, K.W. Dennis, A.M. Russel, R.W. MacCallum Diffusion of Fe, Co, Nd, and Dy in $R_2(Fe_{1-x}Co_x)_{14}B$ where R=Nd or Dy, J. Magn. Magn. Mater. 233 (2001) 136-141.
[82] D. Isheim, M.S. Gagliano, M.E. Fine, D.N. Seidman, Interfacial segregation at Cu rich precipitates in a high-strength low-carbon steel studied on a sub-nanometer scale, Acta Mater. 54 (2006) 841-849.
[83]K. Fritz, B. Grieb, E.T. Henig, G. Petzow, The Influence of Dy on the Phase Relations of (Nd,Dy)–Fe–B Alloys, Z. Metallkd. 83 (1992) 157-161.
[84] M.A. Van Ende, I. Jung, Y.H. Kim, T.S. Kim, Thermodynamic optimization of the Dy–Nd–Fe–B system and application in the recovery and recycling of rare earth metals from NdFeB magnet, Green Chem. 17 (2015) 2246-2262.
[85] X.B. Liu, Z. Altounian, The partitioning of Dy and Tb in NdFeB magnets: A first-principles study, J. Appl. Phys. 111 (2012) 07A701.
[86] H. Kronmüller, K.D. Durst, M. Sagawa, Analysis of the magnetic hardening mechanism in RE-FeB permanent magnets, J. Magn. Magn. Mater. 74 (1988) 291-302.
[87] D.W. Lim, H. Kato, M. Yamada, G. Kido, Y. Nakagawa, High-field magnetization process and spin reorientation in $(Nd_{1-x}Dy_x)_2Fe_{14}B$ single crystals, Phys. Rev. B 44 (1991) 10014.